A Moments View of Climatology and Variability of the Asian Summer Monsoon Anticyclone

Gloria L Manney*

NorthWest Research Associates & New Mexico Institute of Mining and Technology, Socorro, New Mexico, USA

Zachary D Lawrence†

Cooperative Institute for Research in Environmental Sciences (CIRES), University of Colorado, Boulder Colorado, USA.

Michelle L Santee

Jet Propulsion Laboratory, California Institute of Technology, Pasadena, California, USA.

Krzysztof Wargan

Science Systems and Applications Inc., Lanham, MD, USA & NASA Goddard Space Flight Center, Greenbelt, Maryland, USA.

Michael J Schwartz

Jet Propulsion Laboratory, California Institute of Technology, Pasadena, California, USA.

Corresponding author address: Dept. of Physics, New Mexico Institute of Mining and Technology, Socorro, New Mexico, 87801, USA.

E-mail: manney@nwra.com

†Also at NorthWest Research Associates, Boulder, CO, USA.

ABSTRACT

A moments/area study of meteorological reanalyses (focusing on MERRA-2, ERA-Interim, and JRA-55) allows a novel investigation of the climatology of and interannual variability and trends in the Asian summer monsoon anticyclone (ASMA). The climatological ASMA is nearly elliptical, with its major axis aligned along its centroid latitude and an aspect ratio of ∼5–8. The ASMA centroid shifts northward with height, northward and westward during development, and in the opposite direction as it weakens. ASMA position and seasonal evolution generally agree among the reanalyses, except that MERRA-2 shows over 40% larger area at 350 K. No evidence of climatological bimodality is seen in the ASMA, consistent with previous studies using modern reanalyses. ASMA moments trends are mostly neither statistically significant nor consistent among reanalyses, but area and duration increase significantly over 1979–2018, and over 1958–2018 in JRA-55; JRA-55 trends are largest for 1979–2018, suggesting that reanalysis trends may have accelerated in recent decades. ASMA centroid latitude is significantly negatively (positively) correlated with subtropical jet core latitude (altitude), and significantly negatively correlated with concurrent ENSO. Other ASMA moments and area are not strongly correlated with concurrent ENSO, but ASMA area is significantly positively correlated with ENSO two months previously. Significant (negative) correlations of ASMA area with QBO are seen only during June at 370, 390, and 410 K. These results provide a unique and comprehensive view of the structure and evolution of the ASMA and introduce new tools that can be used to further explore ASMA characteristics and impacts.

1. Introduction

The Asian summer monsoon (ASM) anticyclone (ASMA) is a dominating feature of the boreal summer upper troposphere / lower stratosphere (UTLS) circulation, consisting of a vast upper level anticyclonic vortex bounded by the subtropical westerly jet to the north and the tropical easterly jet (TEJ) to the south (e.g., Dunkerton 1995; Hsu et al. 1999; Zarrin et al. 2010). It is thought to arise primarily as a response to diabatic heating associated with convection over the Tibetan and/or Iranian plateaus (Hoskins and Rodwell 1995; Liu et al. 2004; Randel and Park 2006; Garny and Randel 2013; Ren et al. 2019, and references therein) and exhibits strong intraseasonal and interannual variability that may be related to variations in topographic heating and/or dynamical influences originating from the subtropical jet or the tropics (Garny and Randel 2013; Ren et al. 2019; Wu et al. 2020, and references therein). The ASMA is characterized by a high cold tropopause (e.g., Highwood and Hoskins 1998; Pan et al. 2016; Santee et al. 2017, and references therein), and it is a key factor determining summertime UTLS composition via convective lofting and trapping of near-surface air (e.g., Randel and Park 2006; Bergman et al. 2013; Garny and Randel 2013, 2016; Rauthe-Schöch et al. 2016; Randel and Jensen 2013; Pan et al. 2016; Santee et al. 2017).

Quasi-horizontal exchange of air lofted and initially trapped in the ASMA is an important factor in determining the composition of the lower stratosphere during and following the monsoon season (e.g., Vogel et al. 2014, 2015, 2016; Barret et al. 2016; Müller et al. 2016; Santee et al. 2017; Fadnavis et al. 2018; Gottschaldt et al. 2018; Nützel et al. 2019; Yan et al. 2019; Honomichl and Pan 2020). Impacts of the ASMA on UTLS composition are associated with ASMA-related changes in mixing, Rossby wave breaking, and stratosphere-troposphere exchange (Dethof et al. 1999; Homeyer and Bowman 2013; Tyrlis et al. 2014; Kunz et al. 2015; Abalos et al. 2016; Wu et al. 2018, and references therein). Upper tropospheric ASMA-related circulation variations (such as wind and tropopause changes) have been linked to shifts in tropical cyclone tracks (Kelly et al.

2018) and rainfall variations (e.g., Bollasina et al. 2014; Nützel et al. 2016; RavindraBabu et al. 2019).

Several previous studies focused on the climatology and variability of the ASMA and its composition in a dynamical context: Garny and Randel (2013) used low potential vorticity (PV) regions on the 360 K isentropic surface to relate the seasonal evolution of ASMA area to composition changes and to variability in convective forcing via middle troposphere heating and upper level divergence. Ploeger et al. (2015) developed a new method of identifying the ASMA on the 380 K isentropic surface using PV and its gradients and discussed the properties of the ASMA edge as a transport barrier. Pan et al. (2016) discussed characteristic shapes of the ASMA (some with a bimodal structure) in relation to UTLS trace gas transport. Santee et al. (2017) provided a comprehensive climatology of observed UTLS composition in relation to ASMA location and size.

Several studies of ASMA location and extent have reported evidence for bimodality in the ASMA (with its location defined in various ways, see below), namely preferred locations over the Tibetan and Iranian Plateaus (e.g., Qian et al. 2002; Zhang et al. 2002; Zhou et al. 2009; Zarrin et al. 2010; Yan et al. 2011; Pan et al. 2016). As noted by Nützel et al. (2016) in a review of such studies, the idea has not only been studied extensively to identify mechanisms (Zarrin et al. 2010; Amemiya and Sato 2018; Ren et al. 2019, and references therein) and related transport effects (e.g., Yan et al. 2011), but also has made its way into textbooks. Garny and Randel (2013), using the NASA Global Modeling and Assimilation Office (GMAO) Modern Era Retrospective Analysis for Research and Applications (MERRA) reanalysis, and Ploeger et al. (2015), using the European Centre for Medium Range Weather Forecasts (ECMWF) Interim (ERA-Interim) reanalysis, did not find evidence of bimodality. Noting that many of the studies of bimodality were done using the National Center for Environmental Prediction/National Center for Atmospheric Research reanalysis (NCEP-R1), Nützel et al. (2016) conducted a detailed reanalysis comparison and found strong evidence for bimodality only in NCEP-R1, with no evidence for it in the most

recent generation of modern reanalyses for daily, pentad, or seasonal data, and limited evidence in monthly data. Indeed, as emphasized in numerous studies, NCEP-R1 has long been deprecated for UTLS and stratospheric studies (as has the NCEP/Department of Energy Reanalysis, NCEP-R2, that includes some improvements over NCEP-R1) (see also Pawson and Fiorino 1998; Randel et al. 2000; Manney et al. 2005; Fujiwara et al. 2017; Homeyer et al. 2020; Tegtmeier et al. 2020b,a, and references therein).

Many recent studies, particularly those related to the Stratospheric Processes and their Role in Climate (SPARC)-Reanalysis Intercomparison Project (S-RIP) (Fujiwara et al. 2017), highlight the importance of comparing results derived using multiple reanalyses. Chapters 7 (The Extratropical UTLS) (Homeyer et al. 2020) and 8 (The Tropical Tropopause Layer; includes a section on ASM studies) (Tegtmeier et al. 2020b) in the S-RIP final report (now in production), as well as several papers in the S-RIP *Atmospheric Chemistry and Physics / Earth System Science Datasets* special issue, are particularly relevant to the UTLS (Nützel et al. 2016; Manney et al. 2017; Shangguan et al. 2019; Xian and Homeyer 2019; Tegtmeier et al. 2020a; Wright et al. 2020). Manney and Hegglin (2018) showed that it was critical to evaluate multiple reanalyses (even when using only the most recent high-resolution ones) to help determine the robustness of trends in the UTLS jet streams. Wright et al. (2020) show some biases in tropical and subtropical UTLS temperature structure that may be relevant to understanding ASMA differences. As noted above, much previous work on ASMA climatology and variability has relied on NCEP-R1 and/or NCEP-R2, including many papers published since Nützel et al. (2016) showed those reanalyses to be suspect for examining ASMA structure; these include papers that study aspects of ASMA behavior for which those properties are critical (e.g., Preethi et al. 2017; Ren et al. 2019; Basha et al. 2020; Wu et al. 2020).

Studies of variability and trends in the ASM have often focused on surface or near-surface fields such as rainfall and low-level temperatures or winds (e.g., Kajikawa et al. 2012; Preethi et al.

2017; Kodera et al. 2019; Brönnimann et al. 2016; Wu et al. 2020, and references therein). These include investigations of intraseasonal variations on quasi-biweekly and longer scales (Wang and Duan 2015; Ren et al. 2019; Amemiya and Sato 2018, and references therein). Kajikawa et al. (2012), using rainfall and water vapor flux data, showed evidence of earlier monsoon onset in recent decades. Preethi et al. (2017) examined variability and trends in the south Asian and east Asian sub-systems of the ASM using primarily rainfall, surface pressure, and lower tropospheric winds; they noted a westward shift since the 1970s in diagnostics indicative of monsoon activity, and a consistent westward shift in the UT anticyclonic circulation. Bollasina et al. (2013, 2014) suggested that observed earlier onset of monsoon rainfall is related to changes in anthropogenic aerosol radiative forcing. Other papers have also discussed earlier monsoon onsets in surface diagnostics (see, e.g., the review by Bombardi et al. 2020). RavindraBabu et al. (2019) looked at the relationship between interannual variability in ASM onset (based on a precipitation index) and signatures in tropopause variations. Wu et al. (2020) related location shifts and advanced monsoon onset to weakening of the midlatitude UT jet stream. Since the ASMA circulation is bounded on the poleward side by the UT subtropical jet and on the equatorward side by the TEJ, the climatology, variability, and trends of the ASMA are expected to be closely linked to those of the jets, consistent with previous studies of UT jets that show ASMA influences (Schiemann et al. 2009; Manney et al. 2014; Manney and Hegglin 2018, and references therein).

Numerous studies have explored the relationships between interannual variability in the ASM and varying sea surface temperatures (SSTs), including El Niño / Southern Oscillation (ENSO) (e.g., Ju and Slingo 1995; Wang et al. 2001; Tweedy et al. 2018; Yan et al. 2018; Basha et al. 2020; Bombardi et al. 2020, and references therein) and other modes of SST variability. Kodera et al. (2019) explored causes of decadal changes in the ASM and associated SSTs and suggested that recent SST changes strengthened convection penetrating the tropical tropopause layer (TTL) and in turn influenced the stratospheric circulation. Because of the variety of indices, includ-

ing local to regional metrics, used to define monsoon characteristics such as onset and intensity (see, e.g., Bombardi et al. 2020, for a review), the use of several ENSO indices, and the exploration of different lags and time periods for correlations of ENSO with ASM features, studies of ASM relationships to ENSO show no consensus, and indeed the complexity of both the definition of monsoon indices and monsoon/ENSO relationships has been recognized for at least the past several decades (e.g., Webster and Yang 1992). Several studies have observed or simulated an association of preceding El Niño conditions with later monsoon onset and/or weaker monsoon activity (e.g., Ju and Slingo 1995; Webster et al. 1998; Wang et al. 2013; Basha et al. 2020, and references therein), including some studies using ASM intensity indices related to the upper tropospheric circulation (e.g., Tweedy et al. 2018; Yan et al. 2018). However, counter-examples and dependence on ENSO type are also reported (e.g., Yuan and Yang 2012; Wang et al. 2013; Hu et al. 2020). Moreover, recent work suggests changes in the relationship between ENSO and the ASM since the 1990s (e.g., Hrudya et al. 2020; Samanta et al. 2020, and references therein).

The relationships between ASM variations and the quasi-biennial oscillation (QBO) have also been studied (e.g., Giorgetta et al. 1999; Claud and Terray 2007), again with some apparent discrepancies in the results engendered by the diversity of metrics and indices used. While a number of studies suggest a positive correlation between QBO and ASM intensity (e.g., Mukherjee et al. 1985; Giorgetta et al. 1999), others studies have not found consistent correlations (e.g. Claud and Terray 2007; Brönnimann et al. 2016).

Various metrics have been used to identify the ASMA boundary and/or center location, including 100 or 200 hPa geopotential height (GPH) or its gradients (Zarrin et al. 2010; Nützel et al. 2016; Pan et al. 2016, and references therein), GPH anomalies (e.g., Barret et al. 2016), PV thresholds (Garny and Randel 2013; Ploeger et al. 2015; Amemiya and Sato 2018, and references therein), streamfunction (e.g., Tweedy et al. 2018; Yan et al. 2018), and Montgomery Streamfunction (MSF) (e.g., Popovic and Plumb 2001; Fairlie et al. 2014; Santee et al. 2017). The ridgeline of the ASMA

circulation is often identified using relative vorticity, GPH, or wind changes (e.g., Zhang et al. 2002; Zarrin et al. 2010; Nützel et al. 2016). Also see Santee et al. (2017) and Yan et al. (2019) for brief summaries of methods.

Garny and Randel (2013) and Ploeger et al. (2015) both discussed the analogy of the ASMA to the stratospheric polar vortex as a transport barrier, noting that the ASMA can be viewed similarly to that closed circulation in many respects but represents a much "leakier" transport barrier, especially on the equatorward side. Our work follows (and extends) the stratospheric polar vortex analog, but uses MSF on isentropic surfaces as in Santee et al. (2017); as shown therein, one advantage of this metric is that a closed circulation can be defined over a wider range of isentropic levels. We pursue the analogy further by (for the first time to our knowledge) applying a moments and area analysis similar to those that have been effectively used with PV fields to characterize the geometry, vertical structure, preferred locations, and evolution of the stratospheric polar vortex (e.g., Waugh and Randel 1999; Matthewman et al. 2009; Lawrence and Manney 2018).

In this paper, we define the ASMA as in Santee et al. (2017) and use calculations of its moments and area in a comprehensive analysis of its geometry and position and their relationships to natural modes of variability (ENSO and QBO) and to the upper tropospheric subtropical jet. We have conducted the analysis for five of the most recent reanalyses, but focus on the three of those for which we have the longest data records. In Section 2 we describe the reanalysis datasets and methods used. Section 3 presents our results, with an overview (Section 3a); discussions of climatology (Section 3b) and trends (Section 3c1); analysis of correlations with ENSO, QBO, and the subtropical jet (Section 3c2); and investigation of the longer-term record from the most recent reanalysis datasets from the Japan Meteorological Agency (JMA) (Section 3d). Our conclusions are given in Section 4.

2. Data and Methods

a. Reanalysis Datasets

We present the moments and area analysis (see Section 2b below) based on three of the latest generation of "full-input" reanalyses: the GMAO MERRA version-2 (MERRA-2) reanalysis (Gelaro et al. 2017); the ECMWF ERA-Interim reanalysis (Dee et al. 2011); and the JMA 55-year reanalysis (JRA-55) (Ebita et al. 2011; Kobayashi et al. 2015). The models, assimilation systems, and data inputs for those reanalyses are described in detail by Fujiwara et al. (2017). We analyze the climatology and variability of the ASMA moments and area for 1979 through 2018. Calculations are done using daily 12-UT fields from each reanalysis dataset, whose fields are used on their native model levels and at or (in the case of spectral models) near their native horizontal resolution. We thus omit detailed analysis of MERRA, which has been superseded by MERRA-2, and the NCEP CFSR/CFSv2 (Climate Forecast System Reanalysis / Climate Forecast System Version 2), which has been shown to have issues with discontinuities and poorer agreement with observations and other modern reanalyses for many diagnostics (e.g., Long et al. 2017; Manney et al. 2017; Xian and Homeyer 2019). Moreover, CFSR/CFSv2 on native model levels and MERRA are available only through 2015. We have, however, conducted most of the analyses described herein with these two reanalyses for 1979–2015, and figures showing comparisons with them are included in S-RIP Chapter 8 (Tegtmeier et al. 2020b). We use the JRA-55C "conventional input" (that is, no satellite data, see Kobayashi et al. 2014) reanalysis for 1973–2012 to evaluate how JRA-55 might differ in the pre-satellite (before 1979) and satellite periods. This informs our analysis of the full JRA-55 record from 1958–2018.

1) MERRA-2

MERRA-2 (Gelaro et al. 2017), based on the GEOS (Goddard Earth Observing System) assimilation system, uses 3D-Var assimilation with Incremental Analysis Update (IAU) (Bloom

et al. 1996) to constrain the analyses. MERRA-2 data products used here are on model levels and a $0.5^\circ \times 0.625^\circ$ latitude/longitude grid. The 72 hybrid sigma-pressure vertical levels give about 0.8 km vertical spacing in the upper troposphere, increasing to $\sim$1.2 km in the UTLS. Data from MERRA-2 from its spin-up year, 1979, are not in the public record but are included here. We use the MERRA-2 "Assimilated" data collection (Global Modeling and Assimilation Office (GMAO) 2015) here; this data collection is recommended by GMAO for most studies, particularly those that require consistency between mass and wind fields (see, e.g., https://gmao.gsfc.nasa.gov/reanalysis/MERRA-2/docs/ANAvsASM.pdf and Fujiwara et al. 2017). Differences between "Assimilated" and "Analyzed" fields are small but can be non-negligible for some UTLS studies (e.g., Manney et al. 2017); however, comparisons of the two for the moments calculations used herein showed no persistent or significant differences.

2) ERA-INTERIM

ERA-Interim (see Dee et al. 2011) is a global reanalysis covering 1979 through August 2019. The data are produced using 4D-Var assimilation with a T255L60 spectral model. The ERA-Interim data used here are on a $0.75^\circ \times 0.75^\circ$ latitude/longitude grid (near the resolution of the spectral model's Gaussian grid). The 60 model levels have about 1-km spacing in the UTLS.

3) JRA-55

JRA-55 (Ebita et al. 2011; Kobayashi et al. 2015) is a global reanalysis covering 1958 to the present. The data are produced using a 4D-Var assimilation with a T319L60 spectral model. They are provided on an approximately 0.56° Gaussian grid corresponding to that spectral resolution. The JRA-55 fields on the model vertical levels have a vertical resolution and spacing nearly identical to that of ERA-Interim in the UTLS (e.g., see Fig. 3 in Fujiwara et al. 2017). The JRA-55C reanalysis (covering November 1972 through 2012, see, e.g., Kobayashi et al. 2014) uses the same model and grids but does not assimilate satellite data.

b. Methods

1) ASMA CHARACTERIZATION / DIAGNOSTICS

Following Santee et al. (2017), we use contours of daily 1200UT MSF on the 350 K (MSF value 344800 m^2s^{-2}), 370 K (356500 m^2s^{-2}), 390 K (367100 m^2s^{-2}), and 410 K (377300 m^2s^{-2}) isentropic surfaces to define the boundary of the ASMA. Santee et al. (2017) arrived at the listed values by analysis of MSF correlations with windspeed, thus approximating the location of the transport barriers associated with the subtropical westerly and tropical easterly jet cores. The ASMA is identified within the region between 0 and 175° longitude and 0 and 60° latitude (hereinafter the "ASM box"). This box is larger than that used in Santee et al. (2017) and most previous studies (e.g., Bergman et al. 2013; Ploeger et al. 2015; Garny and Randel 2016; Zhang et al. 2016) to ensure that it encompasses the entire ASM region throughout the monsoon season. Extensive inspection of the regions defined as inside the ASMA using this larger box showed no evidence of areas not associated with the ASMA.

The ASMA is characterized through a moments analysis similar to that often used to describe stratospheric polar vortex characteristics (Waugh and Randel 1999; Matthewman et al. 2009; Mitchell et al. 2011; Lawrence and Manney 2018, and references therein) and more generally to describe the geometry of objects (see discussion in Lawrence and Manney 2018). The calculations are based on the algorithms used by Lawrence and Manney (2018) (which in turn followed those of Matthewman et al. 2009), except that the Cartesian grid used is a cylindrical equal area grid covering the ASM box mentioned above, and MSF fields are used instead of PV. As described in detail by Matthewman et al. (2009), this analysis computes the moments of the equivalent ellipse and then uses them to calculate the centroid location (latitude and longitude), aspect ratio, angle, and excess kurtosis (EK); hereinafter we use the term "moments" to describe those derived quantities. EK has been used as a method of identifying polar vortex splits (e.g., Matthewman et al. 2009; Matthewman and Esler 2011). In addition to the moments diagnostics, the area of

the ASMA is calculated as the fraction of the total hemispheric area with MSF greater than the threshold value within the ASM box. Area values less than 1% of a hemisphere are filtered out to limit large day-to-day variability in identification of ASMA existence at the beginning and end of the season because of the presence of very small transient regions about the edge values (similar to the filtering commonly used in stratospheric polar vortex identification, Manney and Lawrence 2016; Lawrence and Manney 2018, and references therein).

The gridpoints at the edge of the ASMA are identified using the Canny edge detection algorithm (Canny 1986). The ASM season is considered to begin (end) when the area with MSF exceeding the boundary value has been greater than 1% of a hemisphere (the general area threshold we use, as mentioned above) for 20 consecutive days prior to (after) the start (end) date. These values were obtained by testing the sensitivity to a range of area (from 0.5% to 2% of a hemisphere) and persistence (from 10 to 30 days) thresholds; the values chosen ensure that the results are not noticeably biased (particularly in the comparison between different reanalyses) by variations in small transient regions above the thresholds.

2) Analysis

In addition to climatological monthly (April through October) and seasonal (June–July–August, JJA) means and frequency distributions of the ASMA edge and centroid locations, we construct climatological time series of the moments, area, and duration diagnostics and examine the distributions of those diagnostics by month over the 40-year period. Timeseries of these diagnostics are examined for potential trends and for correlations with ENSO, QBO, and subtropical UT jet stream variations.

The trend analysis mirrors that of Manney and Hegglin (2018). Apparent trends are identified using a simple linear regression of the monthly and seasonal mean time series of moments and area diagnostics. The statistical significance of the slopes of the linear fits is examined using a permutation analysis (e.g., Wilks 2011, Section 5.3.4) like that described by Manney and Hegglin

(2018), wherein the 40-year time series for each time period (month, season) are randomly shuffled to produce 100,000 possible arrangements of the values, and the linear regression analysis is applied to those. A two-sided p-value is derived by counting how many permuted slopes have larger magnitude than those derived from the reanalyses and dividing by the number of instances (100,000) in the permutation distributions. Consistency among the reanalyses is also critical in assessing the robustness of trends, since one reanalysis may show statistically significant trends opposite to those for others. See Manney and Hegglin (2018) for more detailed discussion.

Relationships with ENSO are assessed using correlations with the Multivariate ENSO Index (MEI, Wolter and Timlin 2011). Relationships with the QBO are examined through correlations with the 50 and 70 hPa Singapore winds provided by the Freie Universität Berlin (Naujokat 1986) and with the 30–50 hPa wind shear. These correlations were also done with ± 2 and ± 1 month lags.

We also examine correlations with the subtropical UT jet streams' latitude, altitude, and windspeed obtained from JETPAC (JEt and Tropopause Products for Analysis and Characterization, Manney et al. 2011a, 2014, 2017; Manney and Hegglin 2018); the subtropical jet is identified (as described by Manney and Hegglin 2018) in a physically meaningful way as the jet across which the "tropopause break" occurs. For this analysis, the zonally averaged jet characteristics, and the jet characteristics averaged over 45–90°E and 80–160°E longitude, have been studied.

To assess the statistical significance of correlations, we use bootstrap resampling (e.g., Elfron and Tibshirani 1993) and resample all the time series 100,000 times. We use this to construct 95 and 99% confidence intervals for the correlations. (See Lawrence et al. 2018; Lawrence and Manney 2020, for further details of the bootstrapping methods).

3. Results

a. Climatological Geometry of ASMA Circulation

Figure 1 shows the climatological mean ASMA edge and centroid locations for each reanalysis (maps are shown in the cylindrical equal area projection used to calculate the moments). Centroid locations generally agree quite well among the reanalyses, especially when the ASMA is fully developed in July and August. The ASMA is larger in MERRA-2 than in the other reanalyses; ERA-Interim typically has the smallest area, but it is closer to that of JRA-55 than JRA-55 is to MERRA-2. The largest differences, at 350 K, arise primarily from a more equatorward southern edge and larger longitudinal extent of the ASMA in MERRA-2. The appearance of only centroid locations (for most reanalyses at most levels in May and September) indicates that mean values were above the edge threshold at only one or two gridpoints. Some MSF values exceed the edge threshold starting in May, but only MERRA-2 at 350 K shows a significant region of such values. In June, the ASMA is larger at 370 K and 390 K than at 350 K and 410 K (as was found by Santee et al. 2017), except in MERRA-2, which shows a much larger area than the other reanalyses at 350 K. Consistent with previous findings based on other measures of ASMA center location and area (e.g., Randel and Park 2006; Bergman et al. 2013; Ploeger et al. 2015; Santee et al. 2017, and references therein), the centroid location shifts north (and in some periods slightly east) with height (e.g., in JJA from below 30°N at 350 K to about 37°N at 410 K), and area in a given time period is largest at 370 K and 390 K (except for MERRA-2 at 350 K in some months). The shift of the centroid location east of the center of the ASMA region in September at 350 and 370 K arises primarily from the common occurrence of a small local maximum to the east, either split off from or attached by a narrow tongue to the main ASMA (e.g., as in eddy-shedding events, Popovic and Plumb 2001; Honomichl and Pan 2020), which affects the centroid location much more than it does the mean edge. For 1979–2015, MERRA areas are similar to those for MERRA-2, and

CFSR/CFSv2 areas are usually slightly smaller than those in the three reanalyses shown herein (S-RIP Chapter 8, Tegtmeier et al. 2020b).

Figure 2, which shows PDFs for JJA from each of the three reanalyses, gives a more detailed view of the ASMA circulation. Both edge and centroid location distributions are broader and less sharply peaked at 350 K than at higher levels. The MERRA-2 350-K centroid distribution is "tilted" east and south with respect to those for ERA-Interim and JRA-55, and its edge distribution is even more diffuse than that of the other reanalyses. All of the reanalyses show a fairly uniform maximum along the southern edge from about 30°E to 120°E. In contrast, there is a localized maximum at the northern edge just west of 90°E (though not as consistently, and barely apparent in MERRA-2, at 350 K), indicating a preferred position along that edge. This position ($\sim$40°N, $\sim$85°E, near the northern edge of the Tibetan Plateau) coincides with the preferred location of the subtropical westerly jet in JJA (Manney et al. 2014) and is consistent with the approximate position of the northern edge towards the eastern side in three of the four "phases" of the ASMA described by Pan et al. (2016).

Except at 350 K, the distributions for the three reanalyses agree well, but with the larger MERRA-2 area reflected in the edge distributions. No clear evidence of bimodality is seen in the centroid or edge locations; this is also the case for PDFs for individual months (not shown). This supports the analysis of Nützel et al. (2016) showing strong bimodality in NCEP-R1 and NCEP-R2 (which are deprecated for most studies including those of the UTLS, see, e.g., S-RIP Chapters 7 and 8, Homeyer et al. 2020; Tegtmeier et al. 2020b, and references therein) but not in modern reanalyses including MERRA, ERA-Interim, and JRA-55. Our conclusions are also consistent with the lack of a clear bimodality signature in other studies using more recent reanalyses (e.g., Garny and Randel 2013; Ploeger et al. 2015). Because ours is a climatological result, it does not preclude the occurrence of bimodal geometries (such as the "Tibetan Plateau", "Iranian

Plateau", or "Double-center" phases shown by Pan et al. 2016) over short periods or on individual days.

b. Climatology of ASMA Moments and Area

Figure 3 shows the climatological seasonal evolution of the ASMA. Climatologically, the moments diagnostics agree well among the reanalyses at 370, 390, and 410 K once the circulation is well developed. At 350 K, MERRA-2 (and MERRA, not shown) has slightly higher (farther east) centroid longitudes from the beginning of the season into August. MERRA-2 (and MERRA) 350-K centroid latitudes are slightly lower throughout the season, with the largest differences (about 5°) early and late in the season.

The centroid location shifts northward and westward during ASMA development, and southward and eastward after the peak of the ASMA season. Strongest shifts are seen at 350 K, where the climatological position is near 15°N and 120°E in May, near 30°N and 75°E at the beginning of August, and near 25°N and 125°E by October; these shifts are consistent with the 10–15° latitude / ∼30° longitude shifts at 100 hPa noted by Nützel et al. (2016). Mean centroid latitudes at the monsoon peak are about 32, 35, and 37°N at 370, 390, and 410 K, respectively, and the mean longitude at the peak is about 75–80°E at all levels. Although the period during which the ASMA is consistently well defined decreases with increasing height (as seen also in Fig. 1), the area increases faster at 370 and 390 K than at 350 K, so, except in MERRA-2, the areas at these higher levels are larger than that at 350 K by June. (Also see Section 3c for further details on ASMA "lifetime".)

The aspect ratio of the equivalent ellipse for the ASMA is calculated daily in the cylindrical equal area projection in which the maps in Figs. 1 and 2 are shown; the aspect ratio of the ASMA typically ranges between 5 and 10 when the circulation is well defined. At 350 K, the aspect ratio increases from about 3 to 10 in June and then remains flat until gradually decreasing again starting

in mid-September. At the higher levels, the aspect ratio increases gradually from 3–5 to 8–10 through the season (until late-September, mid-September, and mid-August at 370, 390, and 410 K, respectively). Much larger peaks (exceeding 20) for individual dates/years tend to cluster near the end of the season, when splitting or pinching off of sub-vortices more often results in a very elongated ASMA.

The angle of the ASMA (measured from the latitude circle of its centroid) tends to be very near zero (with a range of about $\pm 5^\circ$ except for a few brief periods) when the ASMA is well defined, with a tendency towards slightly negative values before mid-season. Large negative values are commonly seen at 350 K through June, indicating that the eastern side of the ASMA frequently tilts equatorward during this period.

EK is a combination of higher-order moments defined by Matthewman et al. (2009) for stratospheric polar vortex studies such that negative values indicate a shape that is pinched in the middle, zero indicates an elliptical vortex, and positive values indicate a "diamond-shaped" vortex or one with extensive filamentation. Matthewman et al. (2009) and Matthewman and Esler (2011) used sufficiently negative values (-0.1 and -0.6, respectively) to indicate vortex splitting. Except at 350 K, ASMA EK is typically slightly positive; significantly negative values are uncommon in this climatology. Statistics of negative EK by year and month show only a few instances at 370, 390, or 410 K with extended periods of negative EK (e.g., July and August 1989 at 370 and 390 K, not shown). Daily MSF maps at these times (not shown) do indeed indicate that negative EK is associated with a pinched ASMA shape (similar to the "western (Iranian plateau)" or "double-center" phases described in Pan et al. 2016); one of the MSF maxima in these cases is typically near the Iranian Plateau (around 40–60°E longitude), consistent with one of the preferred locations in studies suggesting bimodality (Nützel et al. 2016, and references therein), while the location of the other varies considerably. Instances of a split ASMA are found to occur for negative EK magnitudes as small as about 0.25; on the other hand, the ASMA may be unsplit for negative EK

magnitudes as large as 0.65 (the latter cases are generally associated with quite elongated, sinuous ASMA shapes). Thus, while periods of negative EK may signify a particular ASMA structure, they are uncommon and are not a specific indicator of splitting. Large positive EK values are fairly common, especially near the beginning and end of the season (and would occur in situations similar to the "eastern (Tibetan Plateau)" phase of Pan et al. 2016), but their small effect on climatological EK suggests that they occur only for short periods in individual years (more frequently early and late in the ASM season). The slightly positive mean EK values suggest that the ASMA is most often close to elliptical or has a slight bulge along the minor axis. Further exploration of the details of ASMA structure leading to sporadic large variations in EK may be useful for relating anomalous values to specific features, but the complexity of correlating this diagnostic with consistent patterns is beyond the scope of this paper. We thus leave detailed study of EK variations for future work.

At 370, 390, and 410 K, MERRA-2 (and MERRA, not shown) areas are 15–20% larger than those in the other reanalyses. At 390 and 410 K, ERA-Interim areas are 5–10% smaller than those in JRA-55; CFSR/CFSv2 (see S-RIP Chapter 8, Tegtmeier et al. 2020b, for a 370 K example) areas are similar to or slightly smaller than those in ERA-Interim at all levels. At 350 K, MERRA-2 (and MERRA) areas are typically 40 to nearly 50% larger than those for the other reanalyses, consistent with the edge locations shown in Fig. 1. Reanalysis differences in the ranges are similar to those in the means, and the peaks generally line up in time. The exception is the 350-K MERRA-2 range, which includes more high values at all times, and thus the peaks seen in the mean are less distinct (as is also reflected in more diffuse edge distributions, Fig. 2).

The calculated area indicates that the ASMA starts developing in late April at 350 K and in early May to early June at higher levels (also see Section 3c below). At each level, a peak in the area in mid-May (strongest at 350 and 370 K) is followed by a rapid but brief decrease and then a steady rise until late July/early August. Examination of the late-May peak shows that it arises almost

entirely from three years: 1998, 2010, and 2016. Although the area drops abruptly near the end of May in those years (leading to the appearance of the climatological minimum near the beginning of June), these years remain among those with the largest areas through the peak of the monsoon season (see also Section 3c).

While the ASMA threshold MSF value is reached earlier at 350 K, the area increases more slowly than at higher levels. In MERRA-2 (and MERRA, not shown), the maximum ASMA area is about 12% of a hemisphere at 350 K and about 10% at the higher levels; the other reanalyses show a maximum area of only about 7% at 350 K, and slightly under 10% at the higher levels. For comparison, this maximum area is similar to that of the Arctic stratospheric winter polar vortex in a typical year (see, e.g., Manney et al. 2011b; Manney and Lawrence 2016).

Figure 4 shows histograms of the moments (excepting EK) and area of the ASMA during JJA. Consistent with the position differences seen in Fig. 3, the MERRA-2 centroid longitude and latitude histograms have shapes very similar to those for the other reanalyses, but at 350 K are shifted towards higher (by about 3–7°, see mean lines) longitudes and lower (by about 2–3°) latitudes. The angle and aspect ratio histograms agree well among the reanalyses, except for a slight shift toward lower values in both for MERRA-2 at 350 K. The area distributions are consistent with the previous plots, with MERRA-2 showing a much broader distribution peaked at higher values than the other reanalyses at 350 K and a similarly broad distribution but peaked at higher values (about 15–20% larger mean area) at the other levels.

Overall, the climatological picture agrees closely among the reanalyses at and above 370 K; large differences in area and small differences in the moments at 350 K are partially related to larger variability in the ASMA in MERRA-2 than in the other reanalyses at this level. In the following section, we examine interannual variability and evidence for possible trends in the ASMA moments and area.

c. Variability and Trends

1) INTERANNUAL VARIABILITY AND TRENDS IN THE ASMA

Figure 5 shows 40-year time series of the ASMA moments and area for JJA. Considerable interannual variability is seen in all diagnostics. This variability is qualitatively very consistent in all of the reanalyses, but the differences seen in the climatology are reflected in relative biases between the values, especially at 350 K. The overlaid lines showing linear fits suggest an increasing trend in angle and area at all levels. Possible decreasing trends in centroid latitude and increasing trends in aspect ratio are seen at 350, 370, and 390 K, but are not always consistent among the reanalyses. Centroid longitude trends are generally not consistent among the reanalyses, nor are aspect ratio trends at 350 K.

Figure 6 summarizes the trends in the linear fits to the time series shown in Figure 5. Despite consistent slopes among the reanalyses in most cases, relatively few of the apparent trends are significant at the 95% confidence level based on our permutation analysis. Most of the trends are consistent in sign, except where they are very small and not significant (e.g., centroid latitude and longitude at 370 and 390 K, and longitude at 350 K) or in a few individual cases (e.g., aspect ratio in July and August and angle in September at 350 K). Significant and consistent (among the reanalyses) positive trends in aspect ratio are seen in July at 390 and 410 K and in JJA at 370 and 390 K. Uniformly significant positive trends are also seen in angle at 370, 390, and 410 K in July (but note that the angle remains quite small).

Area shows the most robust and consistent trends, with positive trends in all reanalyses, in all months and the JJA season, and at all levels except 410 K in September. Most of these trends are significant at the 95% confidence level except in September, when only 350 K shows consistently significant trends. JRA-55 trends are also insignificant in August at 390 and 410 K and in June and JJA at 410 K, and ERA-Interim and JRA-55 trends are insignificant in June at 390 K. MERRA-2 area trends are substantially larger than those in the other reanalyses at all levels. We have pre-

viously done this trend analysis for periods with end years of 2014, 2015, and 2017, with very similar results (see S-RIP chapter 8, Tegtmeier et al. 2020b, for 370 K example through 2015), indicating that within the 2014–2018 interval the results are not strongly affected by outliers in the end dates (consistent with the general absence of extreme values at the end points of the time series shown in Fig. 5). MERRA and CFSR/CFSv2 area trends through 2015 are consistent with those in the other reanalyses, with MERRA values similar to those for MERRA-2, and CFSR/CFSv2 values stronger (weaker) than those in ERA-Interim and JRA-55 (MERRA-2 and MERRA) (shown in S-RIP Chapter 8, Tegtmeier et al. 2020b). These results suggest a robust increasing trend in ASMA area over the past 36–40 years. This apparent increasing trend in ASMA area is explored in more detail in a paper in preparation, which shows a relationship to multiple dynamical changes more complex than a simple overall increase in MSF values.

Figure 7 shows formation and decay dates and duration (end minus start date) of the ASMA (see Section 2b for details). Consistent with its larger area, MERRA-2 indicates earlier formation and later decay dates, and a correspondingly longer ASMA lifetime, than the other reanalyses, but the interannual variability is in qualitative agreement among the reanalyses. Larger MERRA-2 differences between levels follow directly from the much larger 350-K area in MERRA-2 than in the other reanalyses. The start dates, end dates, and duration at all levels are fairly similar in ERA-Interim and JRA-55, as are those in MERRA-2 at 370, 390, and 410 K. Mean formation dates are earlier at lower levels in JRA-55 and MERRA-2 (e.g., mean values for JRA-55 – typically the "middle" of the three reanalyses – are 30 May, 30 May, 6 June, and 16 June at 350, 370, 390, and 410 K, respectively). The earliest mean start date for ERA-Interim is 4 June at 370 K. End dates in MERRA-2 and JRA-55 are later at lower levels (e.g., JRA-55 mean of 17 September, 15 September, 10 September, and 3 September at 350, 370, 390, and 410 K, respectively), while the latest ERA-Interim end date is 12 September at 370 K. Together, these results lead to the longest mean duration at 350 K for MERRA-2 and JRA-55 (159 and 110 days, respectively) and

at 370 K for ERA-Interim (100 days). These results are consistent with and help quantify the reanalysis differences in ASMA area shown above. S-RIP Chapter 8 (Tegtmeier et al. 2020b) shows that MERRA formation and decay dates and lifetime through 2015 are usually similar to those for MERRA-2, with a few exceptions, particularly much later formation dates (leading to shorter lifetimes) at 350 K in MERRA than in MERRA-2 in 1992 and 2006. CFSR/CFSv2 values are usually similar to those for ERA-Interim and JRA-55, with a few notable outliers at 350 K, especially a very late formation date in 1985 and late/early formation/decay dates in 1992 that result in unrealistically short (less than a month) ASMA lifetimes in those years (S-RIP chapter 8, Tegtmeier et al. 2020b). Our results differ somewhat from those of Santee et al. (2017), who used the same ASMA definition but studied a shorter time period (2005–2014) and used data from the GMAO "GEOS-5.9.1" operational analysis (which used an earlier version of the GMAO assimilation system than does MERRA-2); they further used different criteria for defining ASMA formation and end dates.

The linear fits in Fig. 7 show trends towards earlier formation dates, later decay dates, and longer lifetimes at all levels, consistent with the area trends discussed above. These trends are much larger at 350 K (37, 53, and 41 days longer in 2018 than in 1979 for MERRA-2, ERA-Interim, and JRA-55, respectively) than at higher levels (ranging from 7 to 24 days 2018−1979 difference, depending on level and reanalysis). Figure 8 summarizes the trends in these linear fits and their significance. As with the area trends, these trends are larger at 350 K than at the higher levels and larger in MERRA-2 than in the other reanalyses. Trends at 410 K are not significant except for MERRA-2 decay dates and lifetime; 390 K trends in all quantities in JRA-55 and in decay date in ERA-Interim are also not significant.

2) ASMA Correlations with Upper Tropospheric Jets, ENSO, and QBO

Figures 9 and 10 show correlations of the ASMA moments and area with the subtropical UT jet core latitude and altitude from JETPAC (Manney et al. 2011a; Manney and Hegglin 2018) in the

80–160° longitude region. Similarly strong correlations are seen in the 45–90° longitude region, and weaker ones of consistent sign are seen in the zonal mean (not shown). Strongest correlations are seen with the ASMA centroid latitude, which generally shows significant positive (negative) correlations with subtropical jet latitude (altitude), with weaker/less significant correlations in September and at the higher levels. Since the core of the subtropical jet sits at about 350 K in the ASMA region (e.g., Manney et al. 2014; Santee et al. 2017), weaker correlations at higher levels, especially at 410 K, are not unexpected. This correlation is consistent with the northward shift of the subtropical jet around the poleward edge of the ASMA (typically to a maximum latitude near 42–45°N) during boreal summer (e.g., Schiemann et al. 2009; Manney et al. 2014; Manney and Hegglin 2018). Fig. 9 also shows some significant correlations of subtropical jet latitude with ASMA angle (strongest at 370 and 390 K in July), negative correlations with ASMA longitude and area at 350 K that are occasionally significant, and a positive correlation with ASMA longitude at 410 K in July. ASMA area is usually positively correlated with subtropical jet altitude (Fig. 10), with significant correlations at 350 and 370 K in July and September, as well as in JJA. That ASMA moments/area correlations with subtropical jet latitude and altitude typically have opposite signs is consistent with the general expectation that the jet altitude and latitude are anti-correlated (Lorenz and DeWeaver 2007; Hartmann et al. 2013; Manney and Hegglin 2018, and references therein). No significant correlations of the ASMA with subtropical jet core windspeed were found (not shown).

Correlations of ASMA moments and area with the concurrent MEI index are shown in Fig. 11. While correlations are consistent among the reanalyses (except when they are very small), with a few exceptions (centroid longitude at 350 and 370 K in July and JJA, respectively; aspect ratio at 370 K in JJA), the only uniformly significant correlations with ENSO are for centroid latitude, which shows a consistent and generally significant anti-correlation with the MEI. These correlations are in line with the ASMA / subtropical jet correlations shown above and the results of

Manney et al. (2020, *in preparation*) showing negative correlations of subtropical jet latitude with ENSO.

While correlations between concurrent ENSO and ASMA area are small, Figure 12 shows significant correlations of ASMA area with the MEI two months previously, especially in June and July (smaller but still significant correlations were found for a one-month lag at 390 and 410 K). Lag correlations for the moments and for other lags were either not significant or much less significant than those for concurrent MEI. Correlations of MEI in DJF, Mar, Apr, and May with monsoon onset dates (defined as in Fig. 7) generally indicate positive but insignificant correlations with DJF and March MEI, and inconsistent results for the other months (not shown); an earlier onset date following El Niño conditions would be consistent with the positive two-month lag correlations with area (which we cannot calculate for May since the ASMA formed that early in only a few years). We note that the three years causing the late-May peak in Fig. 3 (1998, 2010, and 2016) all had El Niño conditions in the preceding March; however, several years with strong preceding El Niño conditions have late ASMA formation dates. Although many previous studies show later onsets and/or weaker monsoons during El Niño conditions, this finding is not universal and few of those studies use upper tropospheric metrics of monsoon onset (see Section 1 for a brief review); it would thus require extensive work to understand how previous results relate to those shown here.

Figure 13 shows correlations of ASMA area with the QBO, defined using 70 hPa and 50 hPa Singapore winds (Naujokat 1986). The moments did not in general show significant correlations with QBO, and results for QBO based on 30–50-hPa wind shear, and lag correlations, were no more illuminating (not shown). Significant negative correlations with area are seen in June at 370, 390, and 410 K and are quite consistent among the reanalyses, except for an insignificant correlation of ASMA area with QBO winds at 370 K in MERRA-2; in September, significant negative correlations with the 70-hPa QBO winds are seen in all reanalyses at 410 K and in JRA-55 at 390 K. Correlations of lagged QBO with ASMA start dates show significant (at or greater than

98% confidence level) positive correlations of May QBO winds at 50 hPa with ASMA formation date (not shown; similar correlations at 70 hPa are not significant).

d. The Longer Term Record: JRA-55

JRA-55, which starts in 1958, lets us examine a longer record of 61 years, provided we can show that the pre-satellite and satellite period data are comparable. We assess that comparability through the JRA-55C reanalysis, which spans late 1972 through 2012 and uses only conventional data inputs. Figure 14 shows the mean centroid and edge locations for JRA-55 and JRA-55C during 1973–2012 compared with the JRA-55 mean for 1979–2018 (same as the purple lines in Fig. 1) and JRA-55 for 1958–2018. Except for slightly larger areas in the 1979–2018 period at 350 and 370 K, these all show very close agreement. Agreement is also good for the other climatological fields; for example, Fig. 15 shows that centroid location and area at 370 K match closely in the same four JRA-55/55C time series (except at the beginning and end of the season when day-to-day variability is largest); similar congruence is seen at other levels (not shown).

The time series for the other moments, start/end dates, and duration in JRA-55 and JRA-55C for the comparable periods (not shown) show similarly close agreement. With this indication of skill for these diagnostics without the inclusion of satellite data, we proceed to examine the evidence for trends in the longer-term record. As was the case for 1979–2018 (see Fig. 6), trends in the moments are generally not significant over any of the periods shown; Fig. 16 shows the results of the trend analysis for ASMA area. Comparing the dark and light purple lines (JRA-55 and JRA-55C, respectively, for 1973–2012) indicates very similar changes, but at 370 K changes are slightly less significant in JRA-55 than in JRA-55C. All four cases show significant area increases at 350 K, except for June in the early years. At 370 K, the late period and the full record show significant trends in June through August and in JJA. Most of the area changes are not significant at the higher levels, except for a few in JRA-55 for 1979–2018.

The trends in ASMA start/end dates and duration (Fig. 17) show consistent patterns, with significant decreases (increases) in start date (end date and duration) at 350 K in all four cases and at 370 K in JRA-55 in 1979–2018 and 1958–2018 (excepting end dates for the latter), as well as largest changes in JRA-55 in the 1979–2018 period.

The above results show that increases in JRA-55 area and duration during 1979–2018 are overall larger and more significant than those in the earlier period, in JRA-55C, and in the full 61-year record. While these results are not conclusive, especially given the changes in reanalysis inputs even over the satellite period (see, e.g., Fujiwara et al. 2017), they do suggest the possibility of a recent acceleration in the upward trend in ASMA area.

4. Conclusions and Discussion

We have analyzed the Asian summer monsoon anticyclone (ASMA) in meteorological reanalyses from a new viewpoint by characterizing the climatology and variability of its moments and area. We defined the ASMA as the region within 0–175°E having MSF greater than threshold values on four isentropic surfaces (350, 370, 390, and 410 K) in the UTLS. Its moments and area were calculated using methods analogous to those developed for the stratospheric polar vortex. This approach provides insight into the seasonal evolution of the geometry and location of the ASMA, long-term trends in those characteristics, and relationships of those characteristics to ENSO, QBO, and the upper tropospheric subtropical westerly jet. We focus on results from the recent MERRA-2, ERA-Interim, and JRA-55 reanalyses, and comment briefly on those from MERRA and CFSR/CFsv2. The primary study period is common to the three reanalyses we focus on, 1979–2018; we also analyzed the full 1958–2018 period of the JRA-55 record.

Climatological features of the ASMA are generally consistent among the reanalyses (including the 1973–2012 JRA-55 and JRA-55C records, and the 1958–2018 JRA-55 record), with good

quantitative agreement except for MERRA-2 (and MERRA) at 350 K. Climatological characteristics include:

- The ASMA is small and highly variable in April/May and September, especially at the higher levels, but at its peak in July/August it occupies ∼10% of the hemisphere.

- Centroid locations agree well among the reanalyses, but with slightly lower latitudes and higher longitudes at 350 K in MERRA-2 (and MERRA) than in the other reanalyses.

- MERRA-2 shows substantially larger variability in centroid latitude and area than the other reanalyses at 350 K.

- ASMA centroid longitudes are lowest and latitudes highest when ASMA area is largest (in early August); the ASMA thus moves westward and northward as it develops and eastward and southward as it decays.

- ASMA centroid latitude increases with height, with a maximum latitude of ∼30°N at 350 K increasing to ∼37°N at 410 K; ASMA centroid longitude is similar at all levels studied, near 80°E at the peak of the monsoon season.

- ASMA area is consistently larger in MERRA-2, especially at 350 K, where it exceeds that in the other reanalyses by ∼40–50%. Work in progress shows this difference to originate partly from a significant vertically localized temperature bias in MERRA-2 near 300 hPa (Gelaro et al. 2017), but further details are the subject of ongoing investigation.

- The ASMA generally forms slightly later and decays slightly earlier at higher levels, persisting longest at 350 or 370 K, depending on the reanalysis. Mean durations (averaged over 1979–2018 and the three reanalyses) are 120, 110, 87, and 77 days at 350, 370, 390, and 410 K, respectively.

- Three years (1998, 2010, and 2016) show large ASMA areas in late May that decrease by the end of the month, leading to an apparent minimum in climatological area in early June.

- ASMA angles are largely confined between $\pm 5^{\circ}$; thus the major axis is closely aligned with the latitude circle of its centroid.

- Negative values of excess kurtosis (EK) are associated with ASMA bimodality or splitting, but are uncommon; the usually slightly positive climatological values indicate that the ASMA is on average nearly elliptical with a slight bulge along the minor axis. Thus, although splits and bimodal structure do occur during some periods, they are not frequent enough to leave an imprint of two preferred locations in the climatology.

- ASMA aspect ratios are typically between 5 and 8 when the circulation is well defined, with values increasing gradually until September at 370 through 410 K.

Many of these features confirm or extend previous work: Similar, but not identical, results regarding changing ASMA position/size with height and time were noted qualitatively by Santee et al. (2017) using the same ASMA definition but a much shorter time period, different dataset, and different methods. Lack of evidence of climatological bimodality is consistent with previous work finding bimodality only in older, deprecated, reanalyses (e.g. Ploeger et al. 2015; Nützel et al. 2016); conversely, brief periods of negative EK indicate that bimodality is occasionally apparent in daily ASMA maps, consistent with reported shape variations (e.g., Pan et al. 2016; Honomichl and Pan 2020). Indeed, the lack of climatological bimodality in centroid frequency distributions may suggest that bimodality is more commonly related to shape variations than to two strongly preferred ASMA core locations. Our findings thus support previous work, and they also provide a new geometrical view of the ASMA climatology.

A trend assessment for the ASMA moments and area indicates that:

- Trends in moments are often inconsistent in magnitude and sometimes in sign among the reanalyses and are generally not statistically significant.

- Increasing trends in ASMA area are seen in all reanalyses but are stronger and more significant in MERRA-2, especially at 350 K. With a few exceptions (September at 370 K and some months and reanalyses at 390 and 410 K), area trends are significant at the 95% confidence level. They are not strongly sensitive to ending year within the 2014–2018 interval.

- Consistent with the area trends, in recent years ASMA formation dates are earlier, decay dates later, and lifetimes longer. These trends are typically largest and most significant at 350 K and are strongest in MERRA-2. Averaged over the reanalyses, the ASMA persisted longer in 2018 than in 1979 by 44, 23, 22, and 12 days at 350, 370, 390, and 410 K, respectively.

- JRA-55C 1973–2012 area and duration trends are slightly larger / more significant than those for JRA-55 for the same period.

- JRA-55 trends are substantially larger and more significant for 1979–2018 than for 1958–2018 or 1973–2012, and trends are not significant at the 95% confidence level at 390 or 410 K (and in many cases not at 370 K) for the latter two periods. These results suggest that trends may have accelerated during the past four decades.

These trends are derived from very different metrics than those in previous studies, thus providing a novel view of the changing ASMA. The trend towards earlier ASMA formation seems consistent with previous work showing evidence of earlier monsoon onset (Kajikawa et al. 2012; Bollasina et al. 2013; Bombardi et al. 2020, and references therein). Area trends are not directly comparable to previous metrics of ASMA size or intensity. A paper in preparation explores the relationships of these trends, and their differences among reanalyses, to changes in MSF, temperature, geopotential height, tropopause variations, and other dynamical fields; preliminary results indicate greater complexity in the causes than a simple overall increase in MSF over the period. Note also that

trends from reanalyses must always be treated with caution because of step-changes in data inputs common to different reanalysis products and differences in how each data assimilation system handles such changes (see, e.g., Oliver 2016; Fujiwara et al. 2017; Long et al. 2017; Manney and Hegglin 2018; Bao and Zhang 2019, and references therein).

Correlations of ASMA characteristics with ENSO, QBO, and the upper tropospheric subtropical jet show:

- The ASMA centroid latitude is significantly positively (negatively) correlated with the subtropical jet core latitude (altitude).
- Correlations of other ASMA moments with subtropical jet characteristics, and of ASMA moments and area with subtropical jet windspeed, are generally not significant.
- ASMA centroid latitude is significantly negatively correlated with concurrent ENSO.
- Other ASMA moments and ASMA area are typically not strongly or significantly correlated with concurrent ENSO, but significant correlations are seen of ASMA area with the MEI index two months earlier, particularly in June/July at 370 and 390 K.
- Correlations of the ASMA moments / area with QBO are usually not significant, except for negative correlations of QBO with area in during June at 370, 390, and 410 K.

These results are consistent with those of Manney et al. (2020, *in preparation*) showing negative (positive) correlations of the subtropical jet latitude (altitude) with ENSO, with the northward jet latitude shift during the ASM season (Schiemann et al. 2009; Manney et al. 2014), and with the expected anticorrelation of jet latitude and altitude (e.g., Lorenz and DeWeaver 2007; Hartmann et al. 2013; Manney and Hegglin 2018). While positive lag correlations of area with ENSO are not obviously consistent with common (but not universal) previous reports of stronger monsoons during La Niña conditions, ASMA area is a very different metric than those typically used, so further exploration of these relationships will be of interest.

The diagnostics studied herein shed new light on interannual variability and trends in the ASMA. Applying similar methods to analysis of the North American summer monsoon circulation may prove illuminating. These diagnostics are also well-suited for studies of day-to-day variability. Exploration of observed intraseasonal variability on multiple timescales would be illuminating, as would detailed analysis of unique characteristics of the ASMA in individual seasons (e.g., a paper in preparation using these methods contrasts the ASMA and observed unusual aspects of composition therein in 2017 with the range of interannual variability). Further exploration of the EK moments diagnostic will also be valuable for such case studies; moreover, it may help quantify common shape variations of the ASMA and identify statistical patterns that arise primarily from those shape changes (as opposed to arising from position or intensity changes).

Work in progress using ASMA moments and area to evaluate additional dynamical diagnostics within, around, and at the edges of the ASMA will provide further insight into dynamical changes underlying the trends, variability, and reanalysis differences described herein.

Many studies of trends and variability in monsoon onset, duration, and intensity focus on rainfall and other surface parameters (which, indeed, are most directly relevant to human impacts); exploring the relationships of these parameters to the upper tropospheric ASMA may provide new insights into the coupling between deep convection and the ASM circulation and between UTLS and surface / lower tropospheric impacts of monsoon variability and trends.

The results presented herein thus provide not only a new view of ASMA climatology and variability, but also a new set of tools for exploring ASMA dynamical and composition variability on a range of timescales and their relationships to surface impacts.

Acknowledgments. We thank the Microwave Limb Sounder team at JPL for computational, data processing, management, and analysis support, especially Brian W Knosp and Ryan A Fuller for data processing and management and Luis Millán for JETPAC development and operational processing; Kirstin Krüger, Susann Tegtmeier, Jonathon Wright, and Matthias Nützel for helpful

comments; and NASA's GMAO, ECMWF, and JMA for providing their assimilated data products. GLM and ZDL were partially supported by the JPL Microwave Limb Sounder team under JPL subcontracts to NWRA and NMT; GLM was also supported by a NASA Atmospheric Chemistry Modeling and Analysis project via a subcontract from JPL. KW was supported by NASA's Modeling, Analysis and Prediction (MAP) program, which also provides support for MERRA and MERRA-2. Work at the Jet Propulsion Laboratory, California Institute of Technology, was done under contract with the National Aeronautics and Space Administration. The datasets used/produced are publicly available, as follows:

- MERRA-2: https://disc.sci.gsfc.nasa.gov/uui/datasets?keywords=%22MERRA-2%22
- ERA-Interim: http://apps.ecmwf.int/datasets/
- JRA-55/JRA-55C: Through NCAR RDA at http://dx.doi.org/10.5065/D6HH6H41
- Monsoon moments products: Contact Zachary D Lawrence (zachary.lawrence@noaa.gov)
- JETPAC products (STJ core characteristics): Contact Gloria L Manney (manney@nwra.com)
- MEI: https://www.psl.noaa.gov/enso/mei.old/
- QBO: https://www.geo.fu-berlin.de/en/met/ag/strat/produkte/qbo/index.html

References

Abalos, M., B. Legras, and E. Shuckburgh, 2016: Interannual variability in effective diffusivity in the upper troposphere/lower stratosphere from reanalysis data. *Q. J. R. Meteorol. Soc.*, **142 (697)**, 1847–1861, doi:10.1002/qj.2779.

Amemiya, A., and K. Sato, 2018: A two-dimensional dynamical model for the subseasonal variability of the Asian monsoon anticyclone. *J. Atmos. Sci.*, **75 (10)**, 3597–3612, doi:10.1175/JAS-D-17-0208.1, URL https://doi.org/10.1175/JAS-D-17-0208.1, https://doi.org/10.1175/JAS-D-17-0208.1.

Bao, X., and F. Zhang, 2019: How accurate are modern atmospheric reanalyses for the data-sparse Tibetan Plateau region? *J. Clim.*, **32 (21)**, 7153–7172, doi:10.1175/JCLI-D-18-0705.1, URL https://doi.org/10.1175/JCLI-D-18-0705.1, https://doi.org/10.1175/JCLI-D-18-0705.1.

Barret, B., B. Sauvage, Y. Bennouna, and E. Le Flochmoen, 2016: Upper-tropospheric CO and O_3 budget during the Asian summer monsoon. *Atmos. Chem. Phys.*, **16 (14)**, 9129–9147, doi:10.5194/acp-16-9129-2016, URL https://www.atmos-chem-phys.net/16/9129/2016/.

Basha, G., M. V. Ratnam, and P. Kishore, 2020: Asian summer monsoon anticyclone: trends and variability. *Atmos. Chem. Phys.*, **20 (11)**, 6789–6801, doi:10.5194/acp-20-6789-2020, URL https://acp.copernicus.org/articles/20/6789/2020/.

Bergman, J. W., F. Fierli, E. J. Jensen, S. Honomichl, and L. L. Pan, 2013: Boundary layer sources for the Asian anticyclone: Regional contributions to a vertical conduit. *J. Geophys. Res.*, **118 (6)**, 2560–2575, doi:10.1002/jgrd.50142, URL https://agupubs.onlinelibrary.wiley.com/doi/abs/10.1002/jgrd.50142, https://agupubs.onlinelibrary.wiley.com/doi/pdf/10.1002/jgrd.50142.

Bloom, S. C., L. L. Takacs, A. M. da Silva, and D. Ledvina, 1996: Data assimilation using incremental analysis updates. *Mon. Weather Rev.*, **124**, 1256–1271.

Bollasina, M. A., Y. Ming, and V. Ramaswamy, 2013: Earlier onset of the Indian monsoon in the late twentieth century: The role of anthropogenic aerosols. *Geophys. Res. Lett.*, **40 (14)**, 3715–3720, doi:10.1002/grl.50719, URL https://agupubs.onlinelibrary.wiley.com/doi/abs/10.1002/grl.50719, https://agupubs.onlinelibrary.wiley.com/doi/pdf/10.1002/grl.50719.

Bollasina, M. A., Y. Ming, V. Ramaswamy, M. D. Schwarzkopf, and V. Naik, 2014: Contribution of local and remote anthropogenic aerosols to the twentieth century weakening of the South Asian Monsoon. *Geophys. Res. Lett.*, **41 (2)**, 680–687, doi:10.1002/2013GL058183, URL https://agupubs.onlinelibrary.wiley.com/doi/abs/10.1002/2013GL058183, https://agupubs.onlinelibrary.wiley.com/doi/pdf/10.1002/2013GL058183.

Bombardi, R. J., V. Moron, and J. S. Goodnight, 2020: Detection, variability, and predictability of monsoon onset and withdrawal dates: A review. *Int. J. Clim.*, **40 (2)**, 641–667, doi:10.1002/joc.6264, URL https://rmets.onlinelibrary.wiley.com/doi/abs/10.1002/joc.6264.

Brönnimann, S., and Coauthors, 2016: Multidecadal variations of the effects of the Quasi-Biennial Oscillation on the climate system. *Atmos. Chem. Phys.*, **16 (24)**, 15 529–15 543, doi:10.5194/acp-16-15529-2016, URL https://acp.copernicus.org/articles/16/15529/2016/.

Canny, J., 1986: A computational approach to edge detection. *IEEE Transactions on Pattern Analysis and Machine Intelligence*, **PAMI-8 (6)**, 679–698, doi:10.1109/TPAMI.1986.4767851.

Claud, C., and P. Terray, 2007: Revisiting the possible links between the quasi-biennial oscillation and the Indian summer monsoon using NCEP R-2 and CMAP fields. *J. Clim.*, **20 (5)**, 773–787, doi:10.1175/JCLI4034.1, URL https://doi.org/10.1175/JCLI4034.1, https://doi.org/10.1175/JCLI4034.1.

Dee, D. P., and Coauthors, 2011: The ERA-Interim reanalysis: configuration and performance of the data assimilation system. *Q. J. R. Meteorol. Soc.*, **137**, 553–597.

Dethof, A., A. O'Neill, J. M. Slingo, and H. G. J. Smit, 1999: A mechanism for moistening the lower stratosphere involving the Asian summer monsoon. *Q. J. R. Meteorol. Soc.*, **125**, 1079–1106.

Dunkerton, T. J., 1995: Evidence of meridional motion in the summer lower stratosphere adjacent to monsoon regions. *J. Geophys. Res.*, **100 (D8)**, 16 675–16 688, doi:10.1029/95JD01263, URL https://agupubs.onlinelibrary.wiley.com/doi/abs/10.1029/95JD01263, https://agupubs.onlinelibrary.wiley.com/doi/pdf/10.1029/95JD01263.

Ebita, A., and Coauthors, 2011: The Japanese 55-year Reanalysis "JRA-55": An interim report. *SOLA*, **7**, 149–152.

Elfron, B., and R. J. Tibshirani, 1993: *An Introduction to the Bootstrap*. No. 57, Monographs on Statistics and Applied Probability, Chapman & Hall.

Fadnavis, S., C. Roy, R. Chattopadhyay, C. E. Sioris, A. Rap, R. Müller, K. R. Kumar, and R. Krishnan, 2018: Transport of trace gases via eddy shedding from the Asian summer monsoon anticyclone and associated impacts on ozone heating rates. *Atmos. Chem. Phys.*, **18 (15)**, 11 493–11 506, doi:10.5194/acp-18-11493-2018, URL https://www.atmos-chem-phys.net/18/11493/2018/.

Fairlie, T. D., J.-P. Vernier, M. Natarajan, and K. M. Bedka, 2014: Dispersion of the Nabro volcanic plume and its relation to the Asian summer monsoon. *Atmos. Chem. Phys.*, **14**, 7045–7057.

Fujiwara, M., and Coauthors, 2017: Introduction to the SPARC Reanalysis Intercomparison Project (S-RIP) and overview of the reanalysis systems. *Atmos. Chem. Phys.*, **17**, 1417–1452, doi:10.5194/acp-17-1417-2017, URL www.atmos-chem-phys.net/17/1417/2017/.

Garny, H., and W. J. Randel, 2013: Dynamic variability of the Asian monsoon anticyclone observed in potential vorticity and correlations with tracer distributions. *J. Geophys. Res.*, **118 (24)**, 13,421–13,433, doi:10.1002/2013JD020908,

URL https://agupubs.onlinelibrary.wiley.com/doi/abs/10.1002/2013JD020908, https://agupubs.onlinelibrary.wiley.com/doi/pdf/10.1002/2013JD020908.

Garny, H., and W. J. Randel, 2016: Transport pathways from the Asian monsoon anticyclone to the stratosphere. *Atmos. Chem. Phys.*, **16 (4)**, 2703–2718, doi:10.5194/acp-16-2703-2016, URL https://www.atmos-chem-phys.net/16/2703/2016/.

Gelaro, R., and Coauthors, 2017: The Modern-Era Retrospective Analysis for Research and Applications, Version-2 (MERRA-2). *J. Clim.*, **30**, 5419–5454, doi:doi:10.1175/JCLI-D-16-0758.1.

Giorgetta, M. A., L. Bengtsson, and K. Arpe, 1999: An investigation of QBO signals in the east Asian and Indian monsoon in GCM experiments. *Climate Dynamics*, **15 (6)**, 435–450, URL https://doi.org/10.1007/s003820050292.

Global Modeling and Assimilation Office (GMAO), 2015: Merra-2 inst3_3d_asm_nv: 3d, 3-hourly,instantaneous, model-level, assimilation, assimilated meteorological fields v5.12.4, greenbelt, md, usa, Goddard Earth Sciences Data and Information Services Center (GES DISC), accessed 1 november 2015. doi:10.5067/WWQSXQ8IVFW8.

Gottschaldt, K.-D., and Coauthors, 2018: Dynamics and composition of the Asian summer monsoon anticyclone. *Atmos. Chem. Phys.*, **18 (8)**, 5655–5675, doi:10.5194/acp-18-5655-2018, URL https://www.atmos-chem-phys.net/18/5655/2018/.

Hartmann, and Coauthors, 2013: *Climate Change 2013: The Physical Science Basis. Contribution of Working Group I to the Fifth Assessment Report of the Intergovernmental Panel on Climate Change*, chap. Observations: Atmosphere and Surface. Cambridge University Press, Cambridge, United Kingdom and New York, NY, USA.

Highwood, E. J., and B. J. Hoskins, 1998: The tropical tropopause. *Q. J. R. Meteorol. Soc.*, **124**, 1579–1604.

Homeyer, C. R., and K. P. Bowman, 2013: Rossby wave breaking and transport between the tropics and extratropics above the subtropical jet. *J. Atmos. Sci.*, **70**, 607–626.

Homeyer, C. R., G. L. Manney, L. F. M. A. C. Boothe, T. Xian, M. A. Olsen, M. J. Schwartz, Z. D. Lawrence, and K. Wargan, 2020: Extratropical upper troposphere and lower stratosphere (ExUTLS). *S-RIP Final Report*, M. Fujiwara, G. L. Manney, L. J. Grey, and J. S. Wright, Eds., chap. 7, in review.

Honomichl, S. B., and L. L. Pan, 2020: Transport from the Asian summer monsoon anticyclone over the western Pacific. *J. Geophys. Res.*, **125 (13)**, e2019JD032 094, doi:10.1029/2019JD032094, URL https://agupubs.onlinelibrary.wiley.com/doi/abs/10.1029/2019JD032094, e2019JD032094 2019JD032094, https://agupubs.onlinelibrary.wiley.com/doi/pdf/10.1029/2019JD032094.

Hoskins, B. J., and M. J. Rodwell, 1995: A model of the Asian summer monsoon. Part I: The global scale. *J. Atmos. Sci.*, **52 (9)**, 1329–1340, doi:10.1175/1520-0469(1995)052⟨1329:AMOTAS⟩2.0.CO;2, URL https://doi.org/10.1175/1520-0469(1995)052⟨1329:AMOTAS⟩2.0.CO;2, https://doi.org/10.1175/1520-0469(1995)052⟨1329:AMOTAS⟩2.0.CO;2.

Hrudya, P. H., H. Varikoden, R. Vishnu, and J. Kuttippurath, 2020: Changes in ENSO-monsoon relations from early to recent decades during onset, peak and withdrawal phases of Indian summer monsoon. *Climate Dynamics*, **55 (5)**, 1457–1471, URL https://doi.org/10.1007/s00382-020-05335-x.

Hsu, H.-H., C.-T. Terng, and C.-T. Chen, 1999: Evolution of large-scale circulation and heating during the first transition of Asian summer monsoon. *J. Clim.*, **12 (3)**, 793–810, doi:10.1175/1520-0442(1999)012⟨0793:EOLSCA⟩2.0.CO;2, URL https://doi.org/10.1175/1520-0442(1999)012⟨0793:EOLSCA⟩2.0.CO;2, https://doi.org/10.1175/1520-0442(1999)012⟨0793:EOLSCA⟩2.0.CO;2.

Hu, P., W. Chen, S. Chen, Y. Liu, and R. Huang, 2020: Extremely Early Summer Monsoon Onset in the South China Sea in 2019 Following an El Niño Event. *Mon. Weather Rev.*, **148 (5)**, 1877–1890, doi:10.1175/MWR-D-19-0317.1, URL https://doi.org/10.1175/MWR-D-19-0317.1, https://journals.ametsoc.org/mwr/article-pdf/148/5/1877/4928037/mwrd190317.pdf.

Ju, J., and J. Slingo, 1995: The Asian summer monsoon and ENSO. *Q. J. R. Meteorol. Soc.*, **121 (525)**, 1133–1168, doi:10.1002/qj.49712152509, URL https://rmets.onlinelibrary.wiley.com/doi/abs/10.1002/qj.49712152509, https://rmets.onlinelibrary.wiley.com/doi/pdf/10.1002/qj.49712152509.

Kajikawa, Y., T. Yasunari, S. Yoshida, and H. Fujinami, 2012: Advanced Asian summer monsoon onset in recent decades. *Geophys. Res. Lett.*, **39 (3)**, doi:10.1029/2011GL050540, URL https://agupubs.onlinelibrary.wiley.com/doi/abs/10.1029/2011GL050540, https://agupubs.onlinelibrary.wiley.com/doi/pdf/10.1029/2011GL050540.

Kelly, P., L. R. Leung, K. Balaguru, W. Xu, B. Mapes, and B. Soden, 2018: Shape of Atlantic tropical cyclone tracks and the Indian monsoon. *Geophys. Res. Lett.*, **45 (19)**, 10,746–10,755, doi:10.1029/2018GL080098, URL https://agupubs.onlinelibrary.wiley.com/doi/abs/10.1029/2018GL080098, https://agupubs.onlinelibrary.wiley.com/doi/pdf/10.1029/2018GL080098.

Kobayashi, C. A., H. Endo, Y. Ota, C. Kobayashi, H. Onoda, Y. Harada, K. Onogi, and H. Kamahori, 2014: Preliminary results of the JRA-55C, an atmospheric reanalysis assimilating conventional observations only. *Sci. Online Lett. Atmos.*, **10**, 78–82.

Kobayashi, S., and Coauthors, 2015: The JRA-55 reanalysis: General specification and basic characteristics. *J. Meteor. Soc. Japan*, **93**, doi:10.2151/jmsj.2015-001.

Kodera, K., N. Eguchi, R. Ueyama, Y. Kuroda, C. Kobayashi, B. M. Funatsu, and C. Claud, 2019: Implication of tropical lower stratospheric cooling in recent trends in tropical circu-

lation and deep convective activity. *Atmos. Chem. Phys.*, **19 (4)**, 2655–2669, doi:10.5194/acp-19-2655-2019, URL https://www.atmos-chem-phys.net/19/2655/2019/.

Kunz, A., M. Sprenger, and H. Wernli, 2015: Climatology of potential vorticity streamers and associated isentropic transport pathways across PV gradient barriers. *J. Geophys. Res.*, **120 (9)**, 3802–3821, doi:10.1002/2014JD022615, URL https://agupubs.onlinelibrary.wiley.com/doi/abs/10.1002/2014JD022615, https://agupubs.onlinelibrary.wiley.com/doi/pdf/10.1002/2014JD022615.

Lawrence, Z. D., and G. L. Manney, 2018: Characterizing stratospheric polar vortex variability with computer vision techniques. *Journal of Geophysical Research: Atmospheres*, **123 (3)**, 1510–1535, doi:10.1002/2017JD027556, URL http://dx.doi.org/10.1002/2017JD027556, 2017JD027556.

Lawrence, Z. D., and G. L. Manney, 2020: Does the Arctic Stratospheric Polar Vortex Exhibit Signs of Preconditioning Prior to Sudden Stratospheric Warmings? *J. Atmos. Sci.*, **77 (2)**, 611–632, doi:10.1175/JAS-D-19-0168.1, URL https://doi.org/10.1175/JAS-D-19-0168.1, https://journals.ametsoc.org/jas/article-pdf/77/2/611/4917744/jas-d-19-0168_1.pdf.

Lawrence, Z. D., G. L. Manney, and K. Wargan, 2018: Reanalysis intercomparisons of stratospheric polar processing diagnostics. *Atmos. Chem. Phys.*, **18**, 13 547–13 579, doi:10.5194/acp-18-13547-2018.

Liu, H. L., E. R. Talaat, R. G. Roble, R. S. Lieberman, D. M. Riggin, and J. H. Yee, 2004: The 6.5-day wave and its seasonal variability in the middle and upper atmosphere. *J. Geophys. Res.*, **109**, D21112, doi:10.1029/2004JD004795.

Long, C. S., M. Fujiwara, S. Davis, D. M. Mitchell, and C. J. Wright, 2017: Climatology and interannual variability of dynamic variables in multiple reanalyses evaluated by the SPARC

926 Reanalysis Intercomparison Project (S-RIP). *Atmos. Chem. Phys.*, **17**, 14,593–14,629, URL
927 https://doi.org/10.5194/acp-17-14593-2017.

928 Lorenz, D. J., and E. T. DeWeaver, 2007: Tropopause height and zonal wind response to
929 global warming in the IPCC scenario integrations. *J. Geophys. Res.*, **112**, D10119, doi:
930 10.1029/2006JD008087.

931 Manney, G. L., and M. I. Hegglin, 2018: Seasonal and regional variations in long-term changes in
932 upper tropospheric jets from reanalyses. *J. Clim.*, **31**, 423–448.

933 Manney, G. L., M. I. Hegglin, W. H. Daffer, M. J. Schwartz, M. L. Santee, and S. Pawson, 2014:
934 Climatology of upper tropospheric/lower stratospheric (UTLS) jets and tropopauses in MERRA.
935 *J. Clim.*, **27**, 3248–3271.

936 Manney, G. L., and Z. D. Lawrence, 2016: The major stratospheric final warming in 2016: disper-
937 sal of vortex air and termination of Arctic chemical ozone loss. *Atmos. Chem. Phys.*, **16 (23)**,
938 15 371–15 396, doi:10.5194/acp-16-15371-2016, URL https://www.atmos-chem-phys.net/16/
939 15371/2016/.

940 Manney, G. L., Z. D. Lawrence, and M. I. Hegglin, 2020: Interannual variability in upper tropo-
941 spheric jets in reanalyses: Relationships to ENSO, *in preparation*.

942 Manney, G. L., and Coauthors, 2005: Diagnostic comparison of meteorological analyses during
943 the 2002 Antarctic winter. *Mon. Weather Rev.*, **133**, 1261–1278.

944 Manney, G. L., and Coauthors, 2011a: Jet characterization in the upper troposphere/lower strato-
945 sphere (UTLS): Applications to climatology and transport studies. *Atmos. Chem. Phys.*, **11**,
946 6115–6137.

947 Manney, G. L., and Coauthors, 2011b: Unprecedented Arctic ozone loss in 2011. *Nature*, **478**,
948 469–475.

Manney, G. L., and Coauthors, 2017: Reanalysis comparisons of upper tropospheric/lower stratospheric jets and multiple tropopauses. *Atmos. Chem. Phys.*, 11 541–11 566.

Matthewman, N. J., and J. G. Esler, 2011: Stratospheric sudden warmings as self-tuning resonances. Part I: Vortex splitting events. *J. Atmos. Sci.*, **68 (11)**, 2481–2504, doi:10.1175/JAS-D-11-07.1, URL https://doi.org/10.1175/JAS-D-11-07.1, https://doi.org/10.1175/JAS-D-11-07.1.

Matthewman, N. J., J. G. Esler, A. J. Charlton-Perez, and L. M. Polvani, 2009: A new look at stratospheric sudden warmings. Part III: Polar vortex evolution and vertical structure. *J. Clim.*, **22**, 1566–1585.

Mitchell, D. M., A. J. Charlton-Perez, and L. J. Gray, 2011: Characterizing the variability and extremes of the stratospheric polar vortices using 2d moment analysis. *J. Atmos. Sci.*, **68**, 1194–1213.

Mukherjee, B. K., K. Indira, R. S. Reddy, and B. V. Ramana Murty, 1985: Quasi-Biennial Oscillation in Stratospheric Zonal Wind and Indian Summer Monsoon. *Mon. Weather Rev.*, **113 (8)**, 1421–1424, doi:10.1175/1520-0493(1985)113⟨1421:QBOISZ⟩2.0.CO;2, URL https://doi.org/10.1175/1520-0493(1985)113⟨1421:QBOISZ⟩2.0.CO;2, https://journals.ametsoc.org/mwr/article-pdf/113/8/1421/4168836/1520-0493(1985)113_1421_qboisz_2_0_co_2.pdf.

Müller, S., and Coauthors, 2016: Impact of the Asian monsoon on the extratropical lower stratosphere: trace gas observations during TACTS over Europe 2012. *Atmos. Chem. Phys.*, **16 (16)**, 10 573–10 589, doi:10.5194/acp-16-10573-2016, URL https://www.atmos-chem-phys.net/16/10573/2016/.

Naujokat, B., 1986: An update of the observed quasi-biennial oscillation of the stratospheric winds over the tropics. *J. Atmos. Sci.*, **43 (17)**, 1873–1877, doi:10.1175/1520-0469(1986)043⟨1873:

AUOTOQ⟩2.0.CO;2, URL https://doi.org/10.1175/1520-0469(1986)043⟨1873:AUOTOQ⟩2.0.CO;2, https://doi.org/10.1175/1520-0469(1986)043⟨1873:AUOTOQ⟩2.0.CO;2.

Nützel, M., M. Dameris, and H. Garny, 2016: Movement, drivers and bimodality of the south Asian high. *Atmos. Chem. Phys.*, **16**, 14,755–14,774.

Nützel, M., A. Podglajen, H. Garny, and F. Ploeger, 2019: Quantification of water vapour transport from the Asian monsoon to the stratosphere. *Atmos. Chem. Phys.*, **19 (13)**, 8947–8966, doi:10.5194/acp-19-8947-2019, URL https://www.atmos-chem-phys.net/19/8947/2019/.

Oliver, E. C. J., 2016: Blind use of reanalysis data: apparent trends in Madden-Julian Oscillation activity driven by observational changes. *Intl. J. Clim.*, **36**, 3458–3468, doi:10.1002/joc.4568, URL http://dx.doi.org/10.1002/joc.4568.

Pan, L. L., S. B. Honomichl, D. E. Kinnison, M. Abalos, W. J. Randel, J. W. Bergman, and J. Bian, 2016: Transport of chemical tracers from the boundary layer to stratosphere associated with the dynamics of the Asian summer monsoon. *J. Geophys. Res.*, **121 (23)**, 14,159–14,174, doi:10.1002/2016JD025616, URL https://agupubs.onlinelibrary.wiley.com/doi/abs/10.1002/2016JD025616, https://agupubs.onlinelibrary.wiley.com/doi/pdf/10.1002/2016JD025616.

Pawson, S., and M. Fiorino, 1998: A comparison of reanalyses in the tropical stratosphere. Part 1: thermal structure and the annual cycle. *Clim. Dyn.*, **14 (9)**, 631–644, doi:10.1007/s003820050246, URL https://doi.org/10.1007/s003820050246.

Ploeger, F., and Coauthors, 2015: A potential vorticity-based determination of the transport barrier in the Asian summer monsoon anticyclone. *Atmos. Chem. Phys.*, **15 (22)**, 13 145–13 159, doi:10.5194/acp-15-13145-2015, URL https://www.atmos-chem-phys.net/15/13145/2015/.

Popovic, J. M., and R. A. Plumb, 2001: Eddy Shedding from the Upper-Tropospheric Asian Monsoon Anticyclone. *J. Atmos. Sci.*, **58 (1)**, 93–104, doi:10.1175/1520-0469(2001)058⟨0093:

995 ESFTUT⟩2.0.CO;2, URL https://doi.org/10.1175/1520-0469(2001)058⟨0093:ESFTUT⟩2.0.
996 CO;2, https://journals.ametsoc.org/jas/article-pdf/58/1/93/3452142/1520-0469(2001)058\
997 _0093_esftut_2_0_co_2.pdf.

998 Preethi, B., M. Mujumdar, R. H. Kripalani, A. Prabhu, and R. Krishnan, 2017: Recent trends and
999 tele-connections among south and east Asian summer monsoons in a warming environment.
1000 *Clim. Dyn.*, **48 (7)**, 2489–2505, doi:10.1007/s00382-016-3218-0, URL https://doi.org/10.1007/
1001 s00382-016-3218-0.

1002 Qian, Y., Q. Zhang, Y. Yao, and X. Zhang, 2002: Seasonal variation and heat preference of
1003 the south Asia high. *Adv. Atmos. Sci.*, **19 (5)**, 821–836, doi:10.1007/s00376-002-0047-3, URL
1004 https://doi.org/10.1007/s00376-002-0047-3.

1005 Randel, W. J., and E. J. Jensen, 2013: Physical processes in the tropical tropopause layer and
1006 their roles in a changing climate. *Nature Geosci.*, **6 (3)**, 169–176, URL https://doi.org/10.1038/
1007 ngeo1733.

1008 Randel, W. J., and M. Park, 2006: Deep convective influence on the Asian sum-
1009 mer monsoon anticyclone and associated tracer variability observed with Atmospheric
1010 Infrared Sounder (AIRS). *J. Geophys. Res.*, **111 (D12)**, doi:10.1029/2005JD006490,
1011 URL https://agupubs.onlinelibrary.wiley.com/doi/abs/10.1029/2005JD006490, https://agupubs.
1012 onlinelibrary.wiley.com/doi/pdf/10.1029/2005JD006490.

1013 Randel, W. J., F. Wu, and D. J. Gaffen, 2000: Interannual variability of the tropical tropopause
1014 derived from radiosonde data and NCEP reanalyses. *J. Geophys. Res.*, **105**, 15,509–15,523.

1015 Rauthe-Schöch, A., and Coauthors, 2016: Trapping, chemistry, and export of trace gases in the
1016 South Asian summer monsoon observed during CARIBIC flights in 2008. *Atmos. Chem. Phys.*,
1017 **16**, 3609–3629, doi:10.5194/acp-16-3609-2016.

RavindraBabu, S., M. Venkat Ratnam, G. Basha, and B. Krishnamurthy, 2019: Indian summer monsoon onset signatures on the tropical tropopause layer. *Atmos. Sci. Lett.*, **20 (3)**, e884, doi:10.1002/asl.884, URL https://rmets.onlinelibrary.wiley.com/doi/abs/10.1002/asl.884, https://rmets.onlinelibrary.wiley.com/doi/pdf/10.1002/asl.884.

Ren, R., C. Zhu, and M. Cai, 2019: Linking quasi-biweekly variability of the south Asian high to atmospheric heating over Tibetan Plateau in summer. *Clim. Dyn.*, **53 (5)**, 3419–3429, doi:10.1007/s00382-019-04713-4, URL https://doi.org/10.1007/s00382-019-04713-4.

Samanta, D., B. Rajagopalan, K. B. Karnauskas, L. Zhang, and N. F. Goodkin, 2020: La Niña's diminishing fingerprint on the central Indian summer monsoon. *Geophys. Res. Lett.*, **47 (2)**, e2019GL086 237, doi:10.1029/2019GL086237, URL https://agupubs.onlinelibrary.wiley.com/doi/abs/10.1029/2019GL086237, https://agupubs.onlinelibrary.wiley.com/doi/pdf/10.1029/2019GL086237.

Santee, M. L., G. L. Manney, N. J. Livesey, M. J. Schwartz, J. L. Neu, and W. G. Read, 2017: A comprehensive overview of the climatological composition of the Asian summer monsoon anticyclone based on 10 years of Aura Microwave Limb Sounder measurements. *J. Geophys. Res.*, **122**, 5491–5514, doi:10.1002/2016JD026408, URL http://dx.doi.org/10.1002/2016JD026408.

Schiemann, R., D. Lüthi, and C. Schar, 2009: Seasonality and interannual variability of the westerly jet in the Tibetan Plateau region. *J. Clim.*, **22**, 2940–2957.

Shangguan, M., W. Wang, and S. Jin, 2019: Variability of temperature and ozone in the upper troposphere and lower stratosphere from multi-satellite observations and reanalysis data. *Atmos. Chem. Phys.*, **19 (10)**, 6659–6679, doi:10.5194/acp-19-6659-2019, URL https://www.atmos-chem-phys.net/19/6659/2019/.

Tegtmeier, S., and Coauthors, 2020a: Temperature and tropopause characteristics from reanalyses data in the tropical tropopause layer. *Atmos. Chem. Phys.*, **20 (2)**, 753–770, doi:10.5194/acp-20-753-2020, URL https://www.atmos-chem-phys.net/20/753/2020/.

Tegtmeier, S., and Coauthors, 2020b: Tropical troposphere layer. *S-RIP Final Report*, M. Fujiwara, G. L. Manney, L. J. Grey, and J. S. Wright, Eds., chap. 8, in review.

Tweedy, O. V., D. W. Waugh, W. J. Randel, M. Abalos, L. D. Oman, and D. E. Kinnison, 2018: The impact of Boreal summer ENSO events on tropical lower stratospheric ozone. *J. Geophys. Res.*, **123 (17)**, 9843–9857, doi:10.1029/2018JD029020, URL https://agupubs.onlinelibrary.wiley.com/doi/abs/10.1029/2018JD029020, https://agupubs.onlinelibrary.wiley.com/doi/pdf/10.1029/2018JD029020.

Tyrlis, E., B. kerlak, M. Sprenger, H. Wernli, G. Zittis, and J. Lelieveld, 2014: On the linkage between the Asian summer monsoon and tropopause fold activity over the eastern Mediterranean and the Middle East. *J. Geophys. Res.*, **119 (6)**, 3202–3221, doi:10.1002/2013JD021113, URL https://agupubs.onlinelibrary.wiley.com/doi/abs/10.1002/2013JD021113, https://agupubs.onlinelibrary.wiley.com/doi/pdf/10.1002/2013JD021113.

Vogel, B., G. Günther, R. Müller, J.-U. Grooß, and M. Riese, 2015: Impact of different Asian source regions on the composition of the Asian monsoon anticyclone and of the extratropical lowermost stratosphere. *Atmos. Chem. Phys.*, **15**, 13,699–13,716.

Vogel, B., and Coauthors, 2014: Fast transport from Southeast Asia boundary layer sources to northern Europe: Rapid uplift in typhoons and eastward eddy shedding of the Asian monsoon anticyclone. *Atmos. Chem. Phys.*, **14**, 12,745–12,762.

Vogel, B., and Coauthors, 2016: Long-range transport pathways of tropospheric source gases originating in Asia into the northern lower stratosphere during the Asian monsoon season 2012. *Atmos. Chem. Phys.*, **16**, 15 301–15 325, doi:10.5194/acp-16-15301-2016.

Wang, B., R. Wu, and K.-M. Lau, 2001: Interannual Variability of the Asian Summer Monsoon: Contrasts between the Indian and the Western North PacificEast Asian Monsoons*. *J. Clim.*, **14 (20)**, 4073–4090, doi:10.1175/1520-0442(2001)014⟨4073:IVOTAS⟩2.0.CO;2, URL https://doi.org/10.1175/1520-0442(2001)014⟨4073:IVOTAS⟩2.0.CO;2, https://journals.ametsoc.org/jcli/article-pdf/14/20/4073/3768288/1520-0442(2001)014_4073_ivotas_2_0_co_2.pdf.

Wang, M., and A. Duan, 2015: Quasi-Biweekly Oscillation over the Tibetan Plateau and Its Link with the Asian Summer Monsoon*. *J. Clim.*, **28 (12)**, 4921–4940, doi:10.1175/JCLI-D-14-00658.1, URL https://doi.org/10.1175/JCLI-D-14-00658.1, https://journals.ametsoc.org/jcli/article-pdf/28/12/4921/4040469/jcli-d-14-00658_1.pdf.

Wang, X., X. Jiang, S. Yang, and Y. Li, 2013: Different impacts of the two types of El Niño on Asian summer monsoon onset. *Env. Res. Lett.*, **8 (4)**, 044 053, doi:10.1088/1748-9326/8/4/044053, URL https://doi.org/10.1088%2F1748-9326%2F8%2F4%2F044053.

Waugh, D. W., and W. J. Randel, 1999: Climatology of Arctic and Antarctic polar vortices using elliptical diagnostics. *J. Atmos. Sci.*, **56**, 1594–1613.

Webster, P. J., V. O. Magaa, T. N. Palmer, J. Shukla, R. A. Tomas, M. Yanai, and T. Yasunari, 1998: Monsoons: Processes, predictability, and the prospects for prediction. *J. Geophys. Res.*, **103 (C7)**, 14 451–14 510, doi:10.1029/97JC02719, URL https://agupubs.onlinelibrary.wiley.com/doi/abs/10.1029/97JC02719, https://agupubs.onlinelibrary.wiley.com/doi/pdf/10.1029/97JC02719.

Webster, P. J., and S. Yang, 1992: Monsoon and ENSO: Selectively interactive systems. *Q. J. R. Meteorol. Soc.*, **118 (507)**, 877–926, doi:10.1002/qj.49711850705, URL https://rmets.onlinelibrary.wiley.com/doi/abs/10.1002/qj.49711850705, https://rmets.onlinelibrary.wiley.com/doi/pdf/10.1002/qj.49711850705.

Wilks, D. S., 2011: *Statistical Methods in the Atmospheric Sciences*. 3rd ed., Elsevier Academic Press, volume 100, International Geophysics Series.

Wolter, K., and M. S. Timlin, 2011: El Niño/Southern Oscillation behaviour since 1871 as diagnosed in an extended multivariate ENSO index (MEI.ext). *Intl. J. Clim.*, **31**, 1074–1087, doi:10.1002/joc.2336, URL http://dx.doi.org/10.1002/joc.2336.

Wright, J. S., and Coauthors, 2020: Differences in tropical high clouds among reanalyses: origins and radiative impacts. *Atmos. Chem. Phys.*, **20 (14)**, 8989–9030, doi:10.5194/acp-20-8989-2020, URL https://acp.copernicus.org/articles/20/8989/2020/.

Wu, C.-H., P.-C. Tsai, and N. Freychet, 2020: Changing dynamical control of early Asian summer monsoon in the mid-1990s. *Clim. Dyn.*, **54 (1)**, 85–98, URL https://doi.org/10.1007/s00382-019-04989-6.

Wu, Y., G. Chen, L. Taylor, and P. Zhang, 2018: On the linkage between the Asian summer monsoon and tropopause folds. *J. Geophys. Res.*, **123 (4)**, 2037–2049, doi:10.1002/2017JD027870, URL https://agupubs.onlinelibrary.wiley.com/doi/abs/10.1002/2017JD027870, https://agupubs.onlinelibrary.wiley.com/doi/pdf/10.1002/2017JD027870.

Xian, T., and C. R. Homeyer, 2019: Global tropopause altitudes in radiosondes and reanalyses. *Atmos. Chem. Phys.*, **19**, 5661–5678.

Yan, R.-C., J.-C. Bian, and Q.-J. Fan, 2011: The impact of the south Asia high bimodality on the chemical composition of the upper troposphere and lower stratosphere. *Atmos. Ocean. Sci. Lett.*, **4 (4)**, 229–234, doi:10.1080/16742834.2011.11446934, URL https://doi.org/10.1080/16742834.2011.11446934, https://doi.org/10.1080/16742834.2011.11446934.

Yan, X., P. Konopka, F. Ploeger, A. Podglajen, J. S. Wright, R. Müller, and M. Riese, 2019: The efficiency of transport into the stratosphere via the Asian and North American summer monsoon

circulations. *Atmos. Chem. Phys.*, **19 (24)**, 15 629–15 649, doi:10.5194/acp-19-15629-2019, URL https://www.atmos-chem-phys.net/19/15629/2019/.

Yan, X., P. Konopka, F. Ploeger, M. Tao, R. Müller, M. L. Santee, J. Bian, and M. Riese, 2018: El Niño Southern Oscillation influence on the Asian summer monsoon anticyclone. *Atmos. Chem. Phys.*, **18 (11)**, 8079–8096, doi:10.5194/acp-18-8079-2018, URL https://www.atmos-chem-phys.net/18/8079/2018/.

Yuan, Y., and S. Yang, 2012: Impacts of different types of El Niño on the east Asian climate: Focus on ENSO cycles. *J. Clim.*, **25 (21)**, 7702–7722, doi:10.1175/JCLI-D-11-00576.1, URL https://doi.org/10.1175/JCLI-D-11-00576.1, https://journals.ametsoc.org/jcli/article-pdf/25/21/7702/4005459/jcli-d-11-00576_1.pdf.

Zarrin, A., H. Ghaemi, M. Azadi, and M. Farajzadeh, 2010: The spatial pattern of summertime subtropical anticyclones over Asia and Africa: A climatological review. *Intl. J. Clim.*, **30 (2)**, 159–173, doi:10.1002/joc.1879, URL https://rmets.onlinelibrary.wiley.com/doi/abs/10.1002/joc.1879, https://rmets.onlinelibrary.wiley.com/doi/pdf/10.1002/joc.1879.

Zhang, K., R. Fu, T. Wang, and Y. Liu, 2016: Impact of geographic variations of the convective and dehydration center on stratospheric water vapor over the Asian monsoon region. *Atmos. Chemistry. Phys.*, **16 (12)**, 7825–7835, doi:10.5194/acp-16-7825-2016, URL https://www.atmos-chem-phys.net/16/7825/2016/.

Zhang, Q., G. Wu, and Y. Qian, 2002: The bimodality of the 100 hPa south Asia high and its relationship to the climate anomaly over east Asia in summer. *J. Meteor. Soc. Japan*, **80 (4)**, 733–744, doi:10.2151/jmsj.80.733.

Zhou, N., Y. Yu, and Y. Qian, 2009: Bimodality of the south Asia high simulated by coupled models. *Adv. Atmos. Sci.*, **26 (6)**, 1226, doi:10.1007/s00376-009-7219-3, URL https://doi.org/10.1007/s00376-009-7219-3.

LIST OF FIGURES

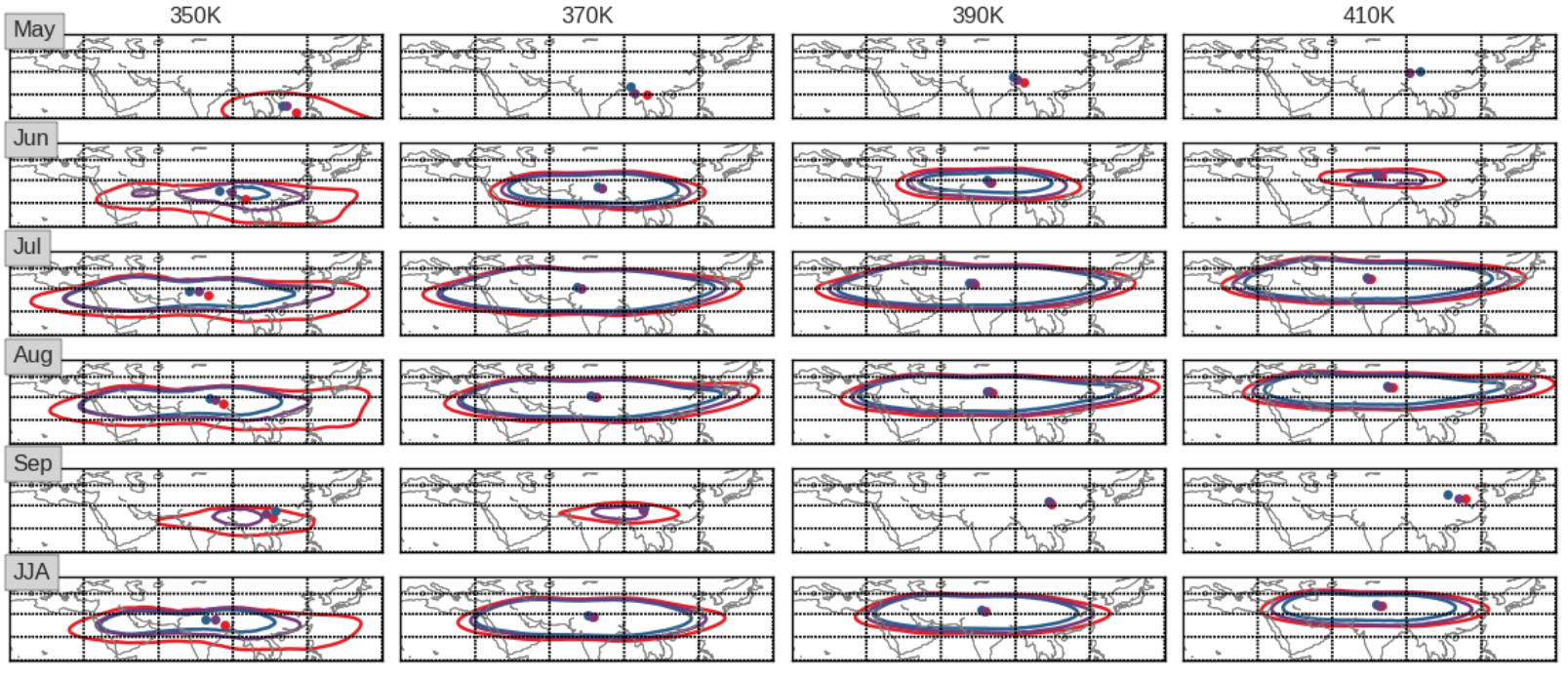

FIG. 1. Climatological (1979 through 2018) means of ASMA edge (contours) and centroid (symbols) locations, for May through September, and JJA, for three reanalyses: MERRA-2 (red), ERA-Interim (blue), and JRA-55 (purple). The isentropic levels are (left to right columns) 350, 370, 390, and 410 K. The longitude domain is 0 to 180°E, with dashed lines every 30°; the latitude domain is 0 to 60°N, with dashed lines every 15°.

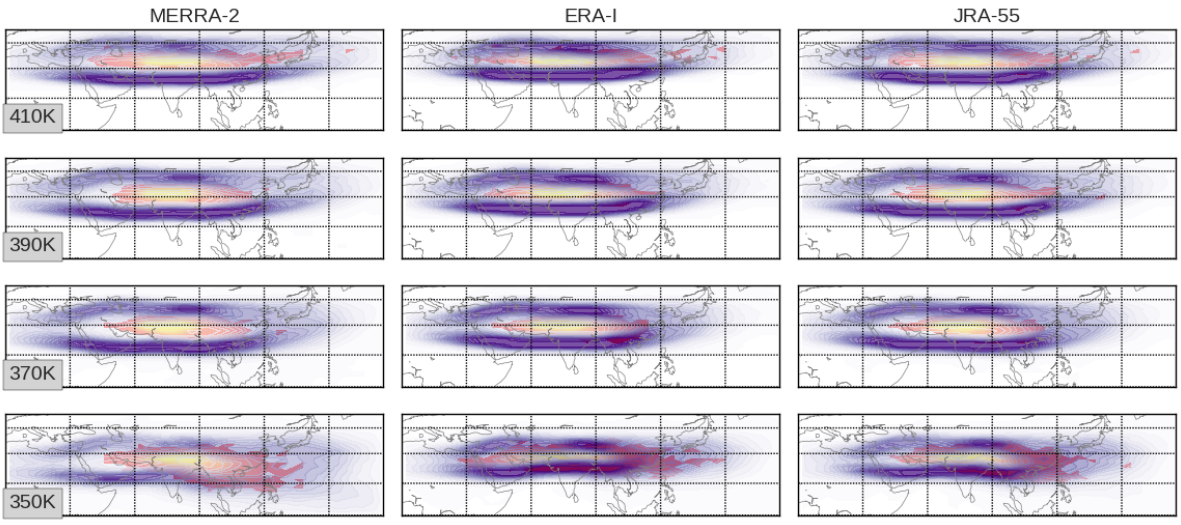

FIG. 2. Climatological (1979 through 2018) frequency distributions of ASMA edge (purples) and centroid (reds/oranges) locations, for JJA, from (left to right) MERRA-2, ERA-Interim, and JRA-55. The isentropic levels are (top to bottom) 410, 390, 370, and 350 K. The longitude domain is 0 to 180°E, with dashed lines every 30°; the latitude domain is 0 to 60°N, with dashed lines every 15°.

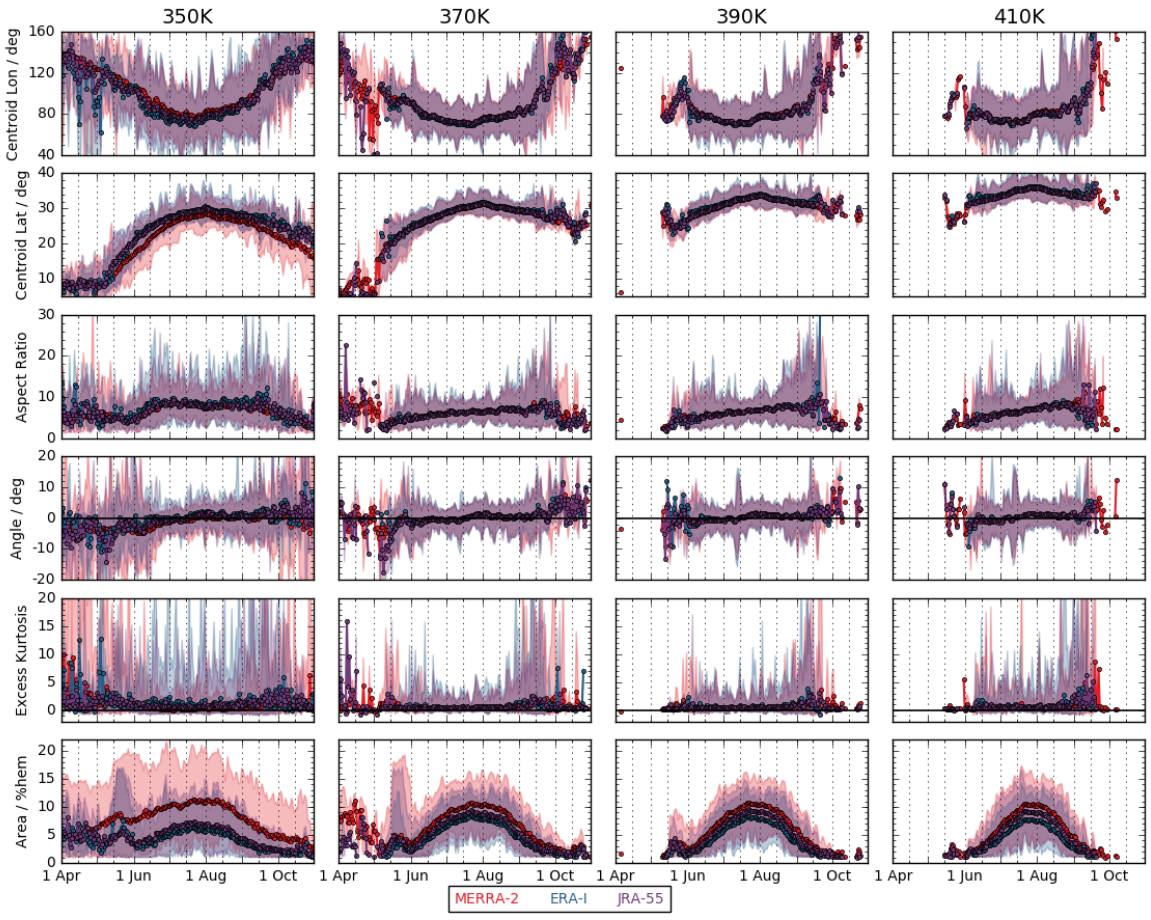

FIG. 3. Climatological (1979–2018) time series of moments and area of the ASMA at (left to right) 350, 370, 390, and 410 K; fields are top to bottom: centroid longitude, centroid latitude, aspect ratio, angle, excess kurtosis, and area. Envelopes show the range of values for the corresponding reanalysis (colors are shown in the legend).

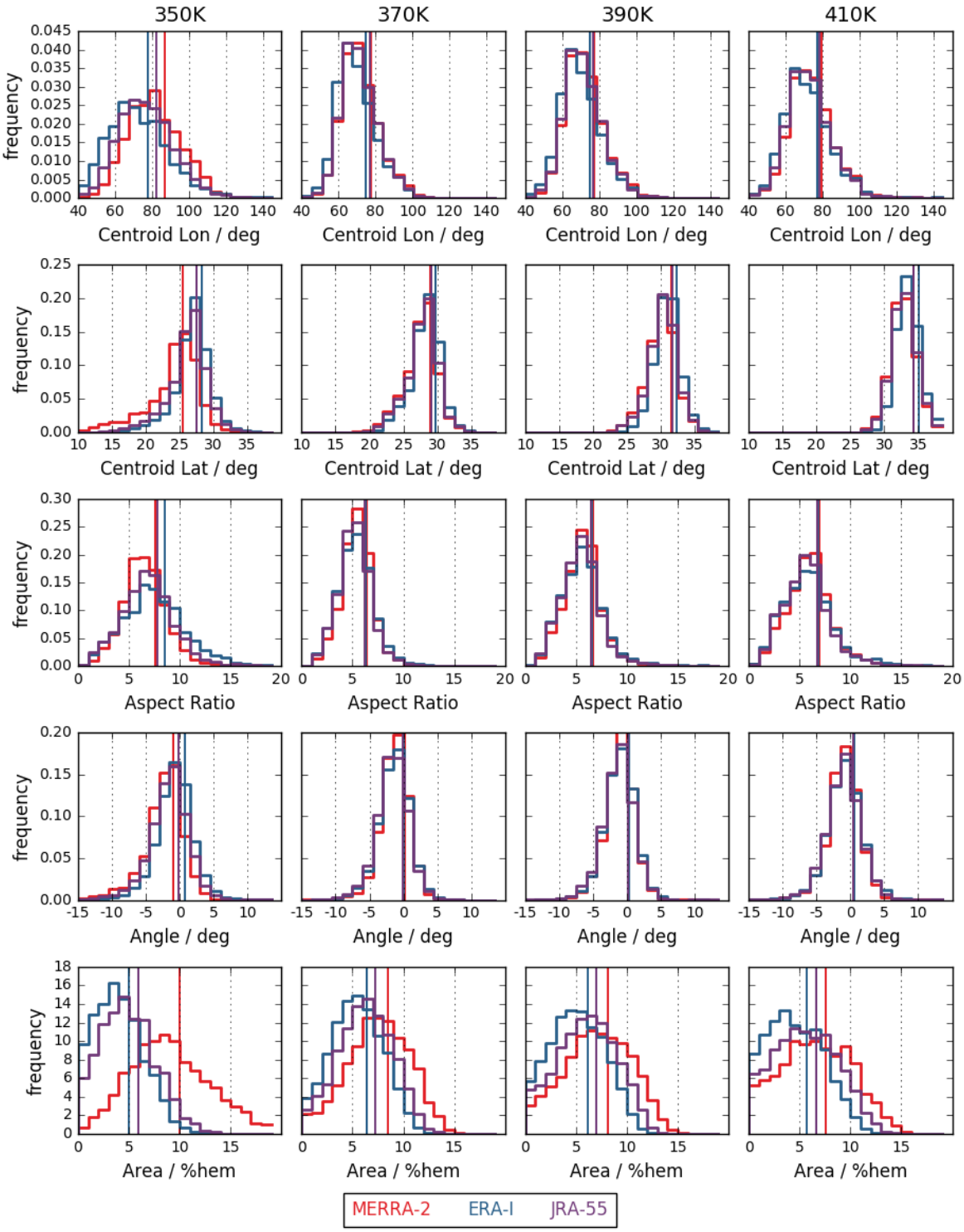

FIG. 4. Histograms of climatological JJA moments and area of the ASMA, top to bottom: centroid longitude, centroid latitude, aspect ratio, angle, and area. Vertical lines show climatological mean for each reanalysis.

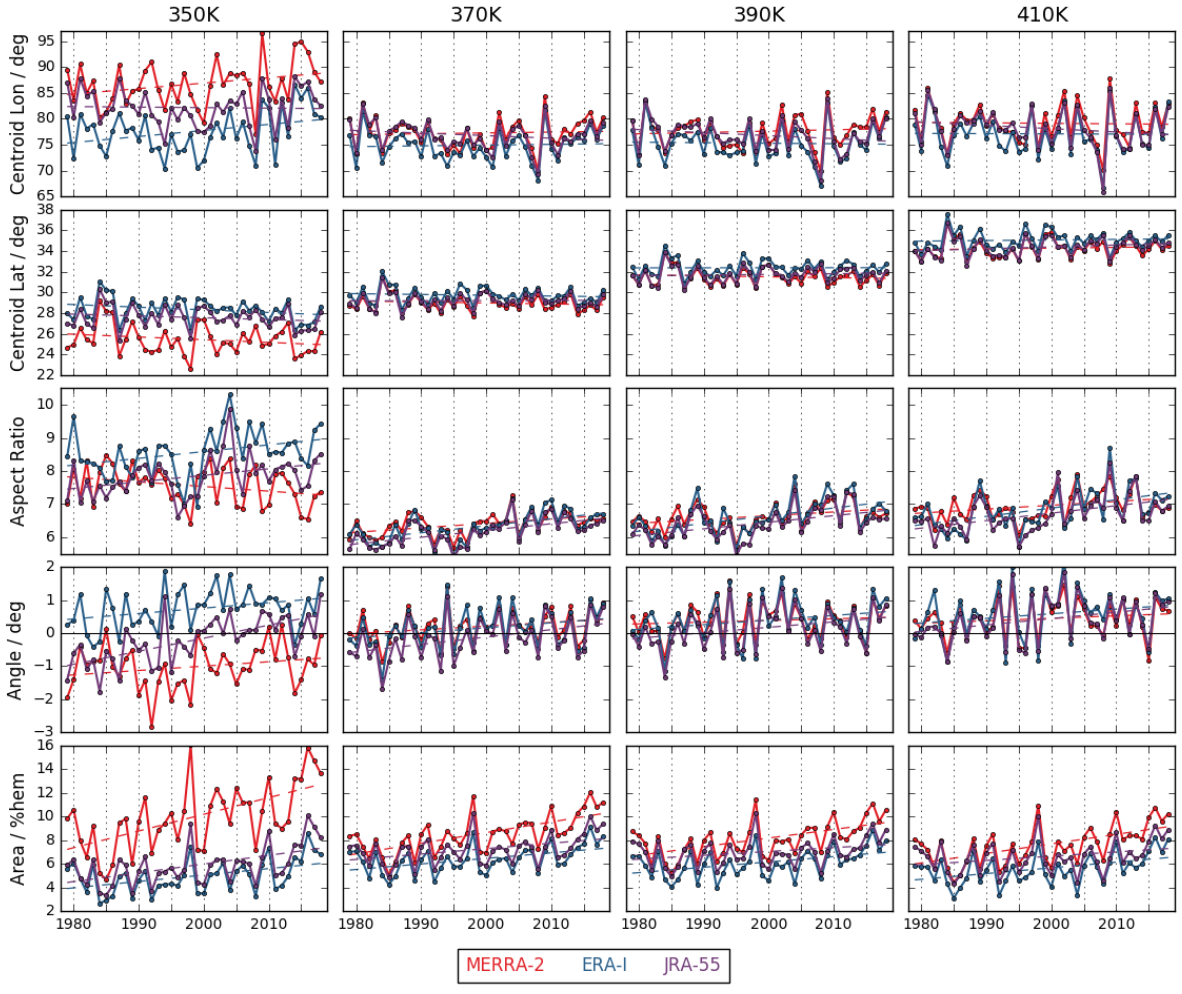

1202 FIG. 5. Time series for 1979 through 2018 of JJA moments and area of the ASMA at (left to right) 350, 370,
1203 390, and 410 K for the three reanalyses; top to bottom: centroid longitude, centroid latitude, aspect ratio, angle,
1204 and area. Overlaid lines show linear fits to the values.

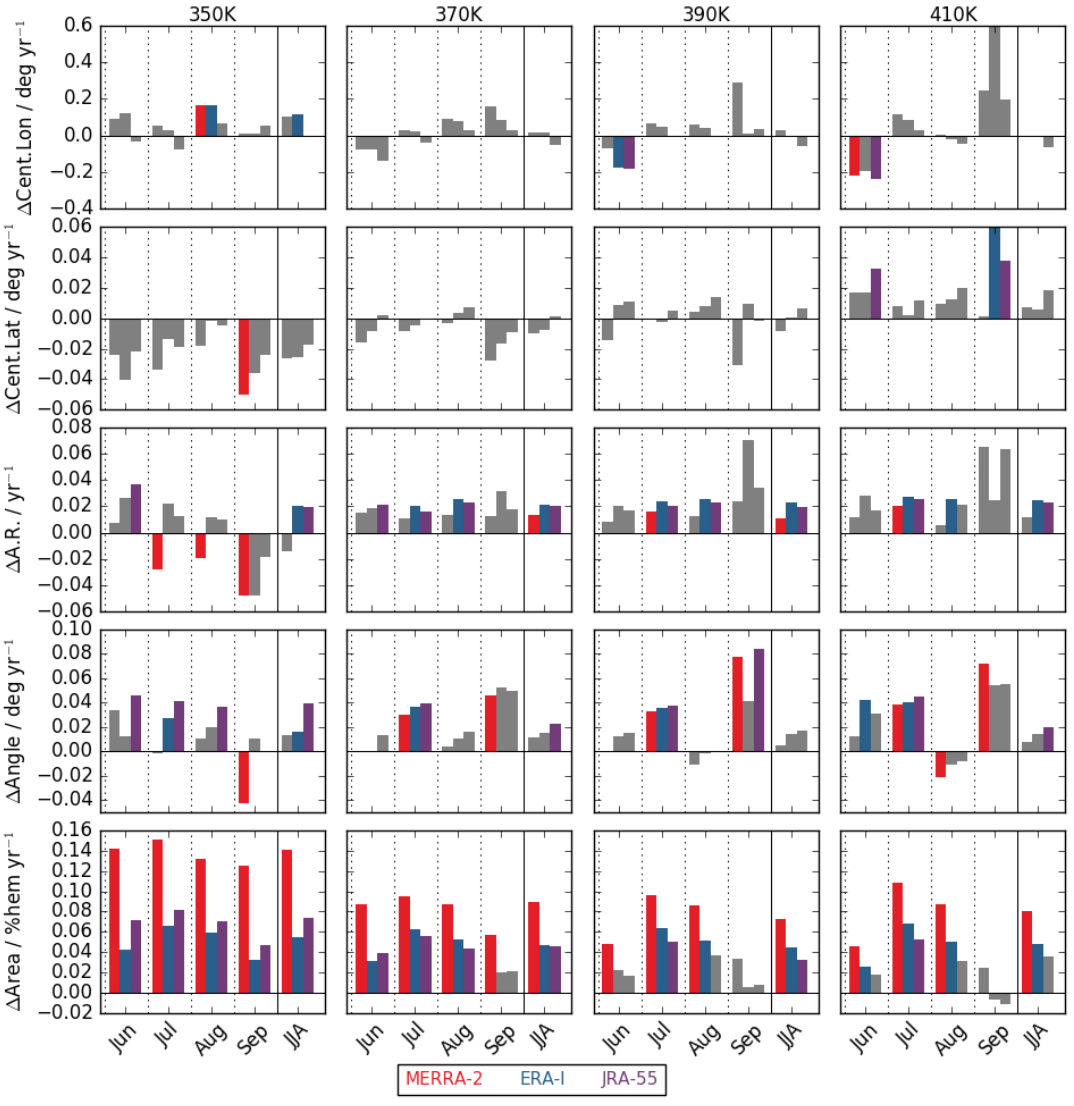

FIG. 6. Slopes of linear fits to the moments and area time series shown in Figure 5. Bars in the reanalysis colors indicate slopes that are significant at the 95% confidence level according to a permutation analysis (see Section 2b).

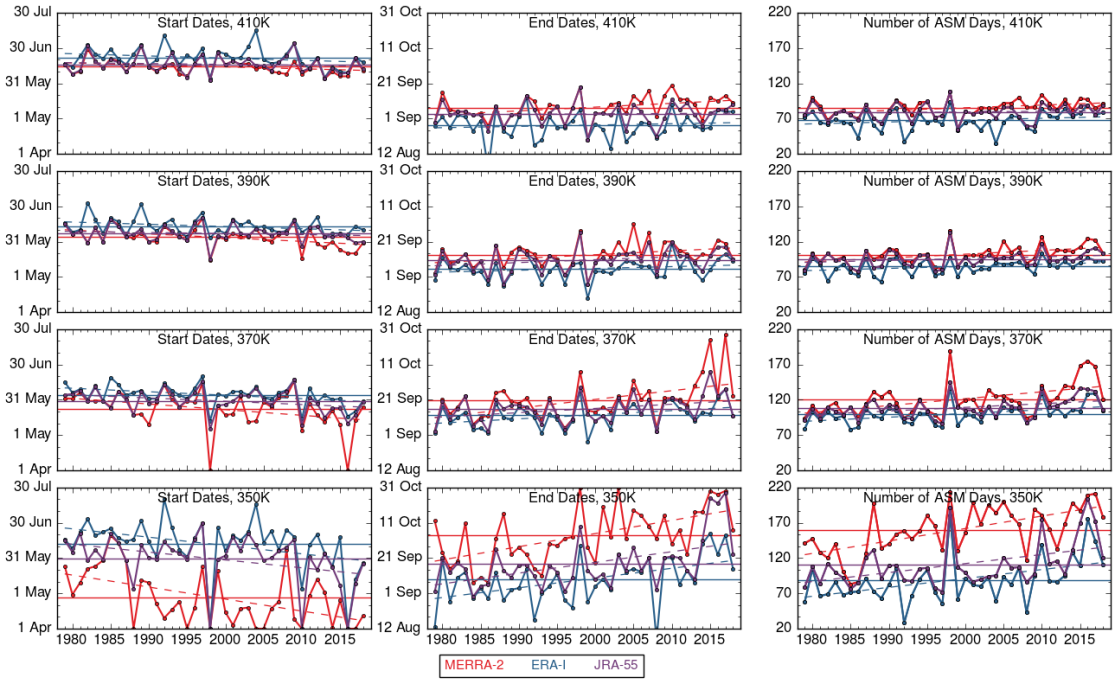

1208 FIG. 7. Start dates, end dates, and duration of the monsoon season as defined in the text (Section 2b). Hori-
1209 zontal lines show each reanalyses' mean over the 40-year period. Overlaid dashed lines show linear fits to the
1210 values.

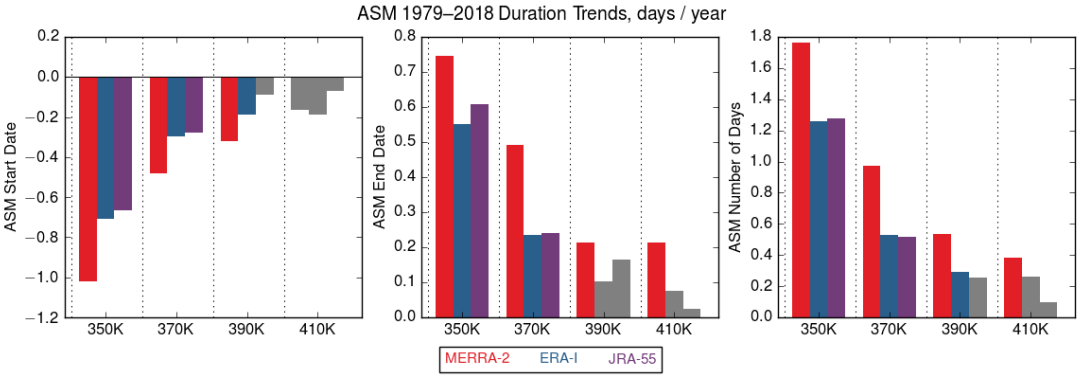

FIG. 8. Slopes of linear fits to the start date, end date, and duration time series shown in Figure 7. Bars in reanalysis colors indicate slopes that are significant at the 95% confidence level according to a permutation analysis (see Section 2b).

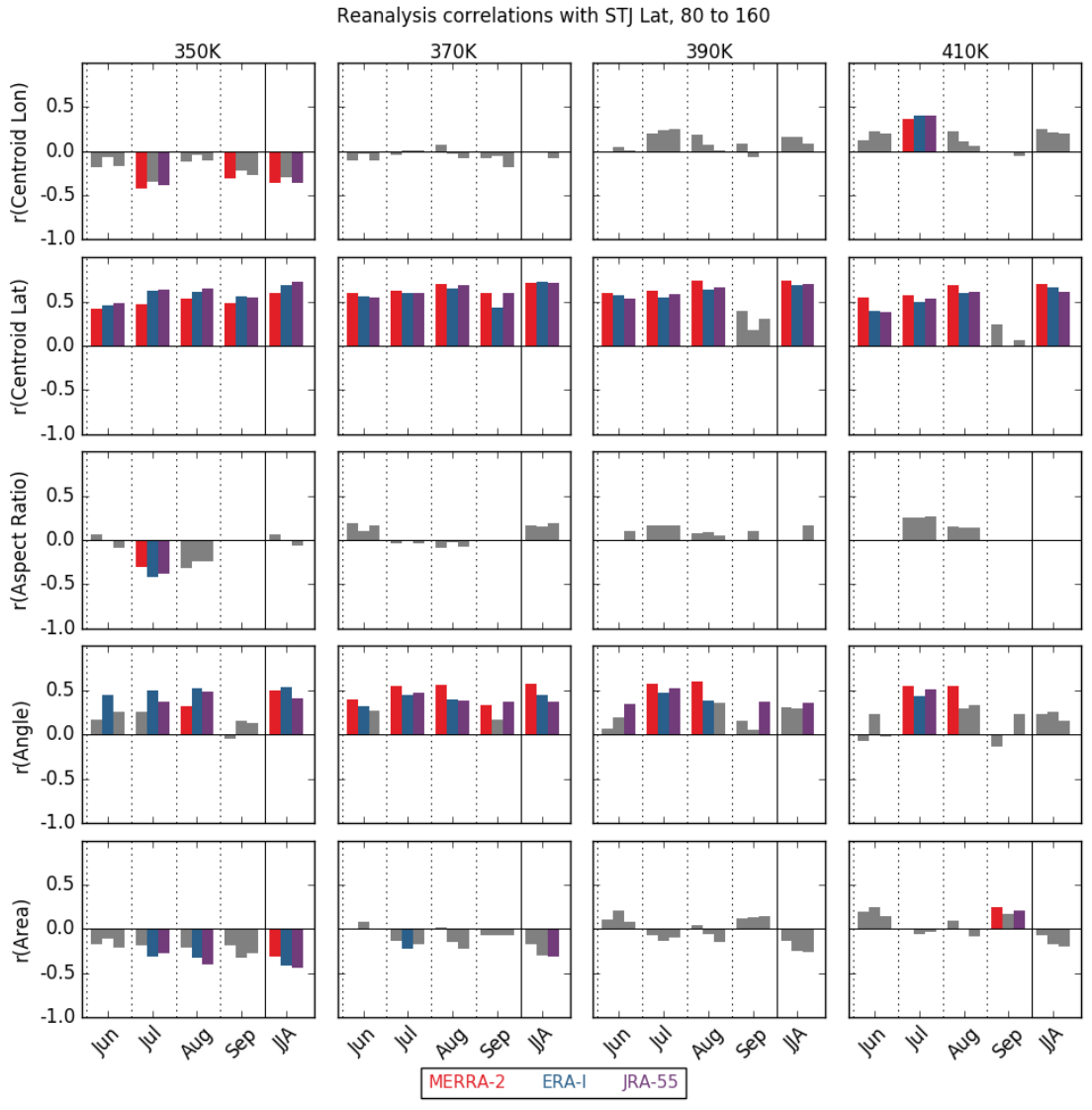

1214 FIG. 9. Correlation between ASMA moments / area and the latitude of the subtropical upper tropospheric jet
1215 (see text for jet characterization methods) in the 80 to 160° longitude band. Correlations that are significant at
1216 the 95% level in a bootstrapping analysis (Section 2b) are shown in the reanalysis colors.

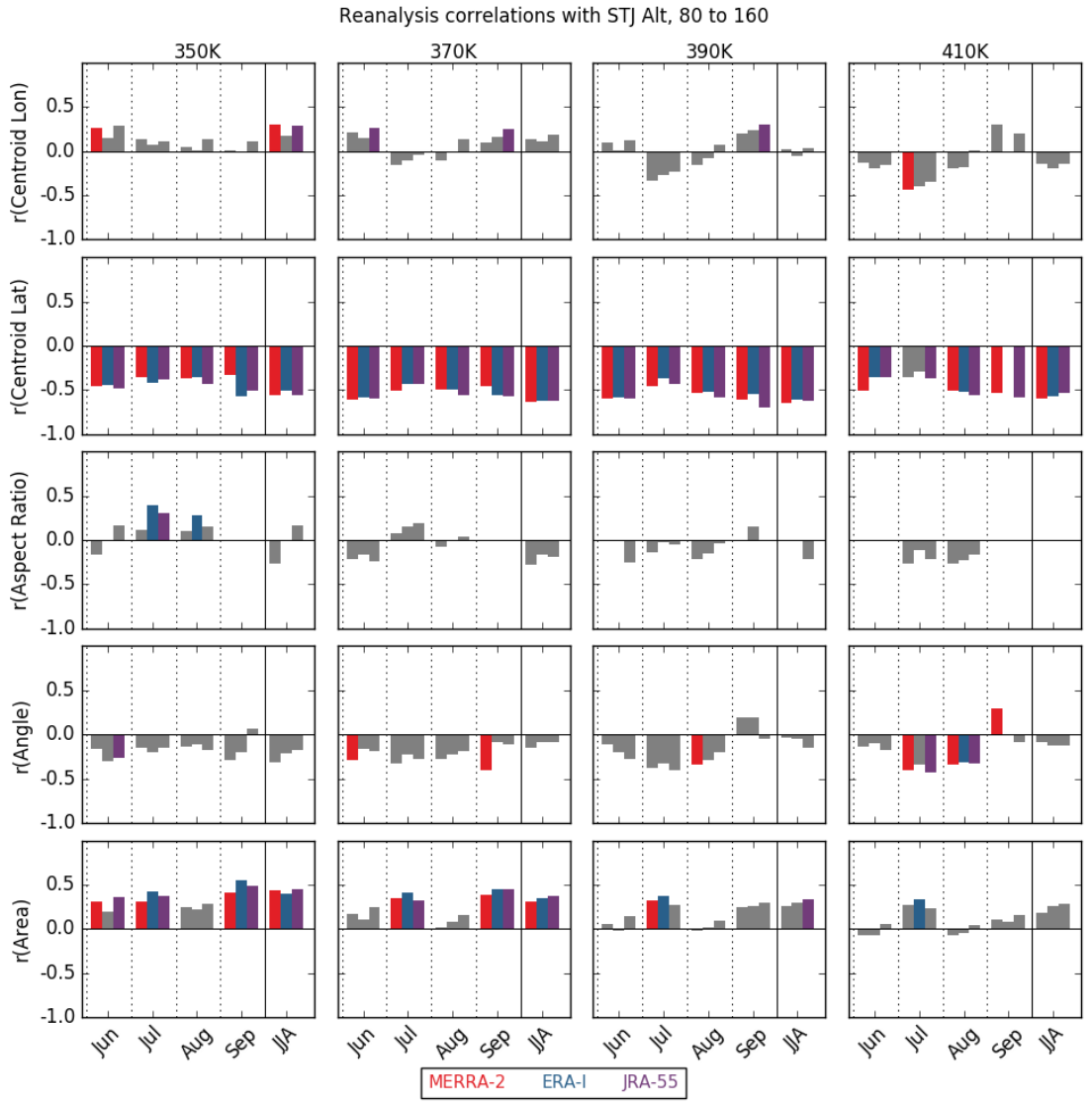

1217 FIG. 10. Correlation between ASMA moments / area and the altitude of the subtropical upper tropospheric
1218 jet (see text for jet characterization methods) in the 80 to 160° longitude band. Correlations that are significant
1219 at the 95% level are shown in the reanalysis colors.

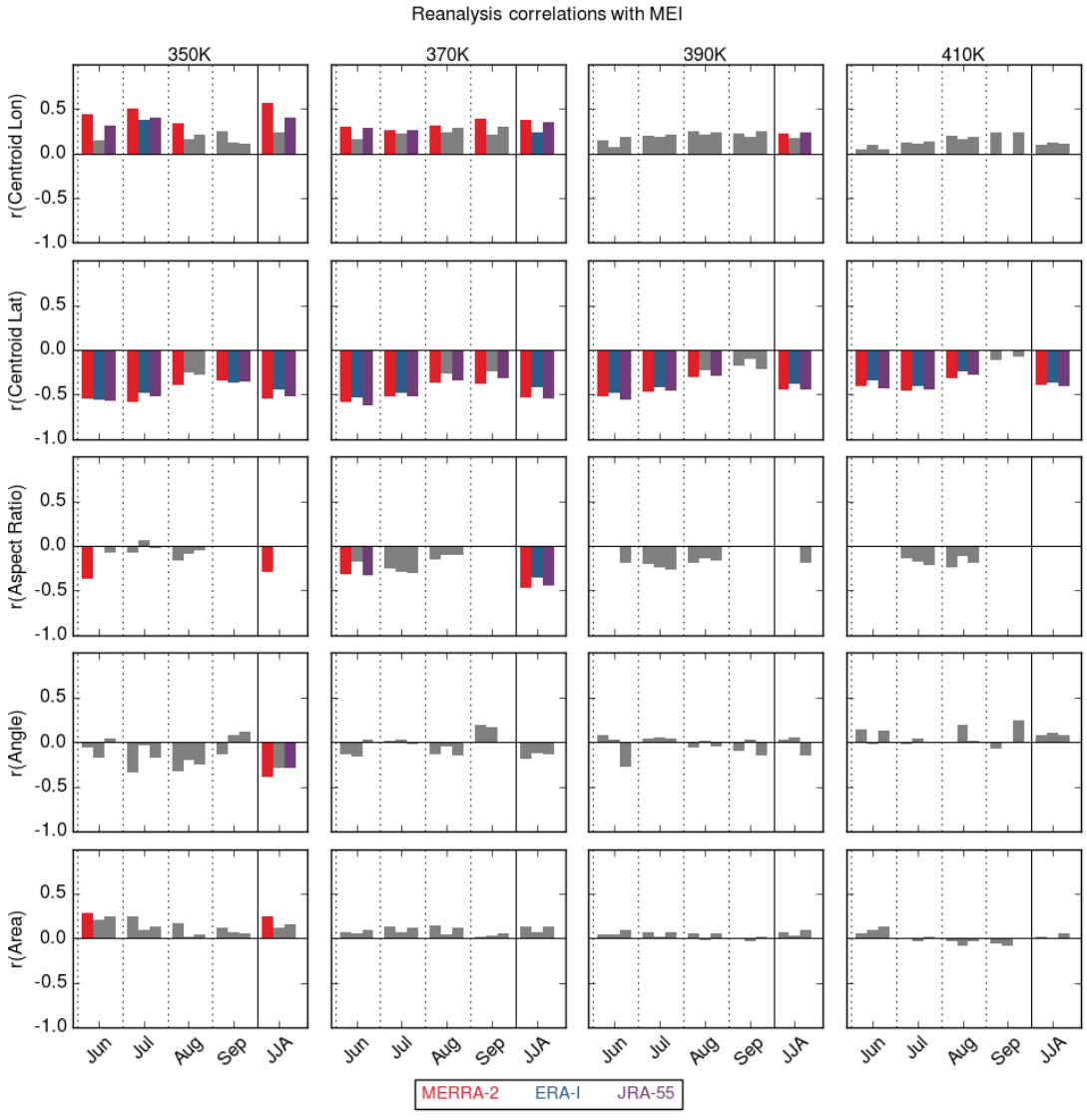

1220 FIG. 11. Correlations between ASMA moments / area and the MEI index. Correlations that are significant at
1221 the 95% confidence level are shown in the reanalysis colors.

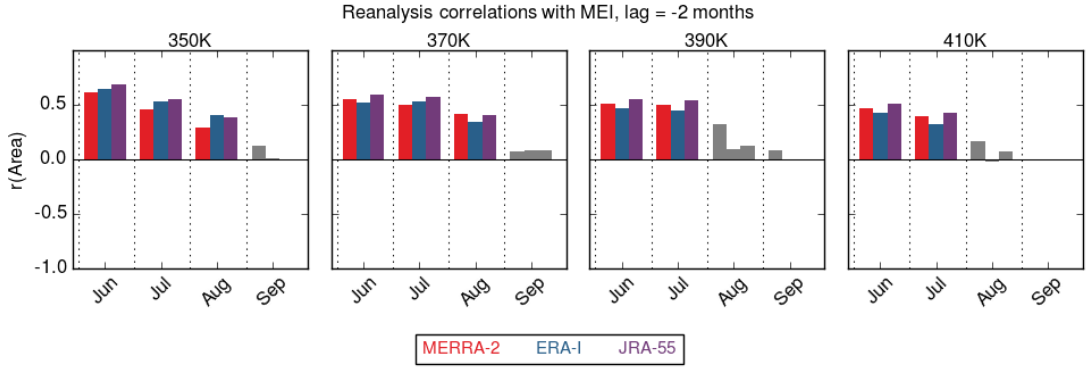

FIG. 12. Correlations between ASMA area and the MEI index with a 2-Month lag. Correlations that are significant at the 95% confidence level are shown in the reanalysis colors.

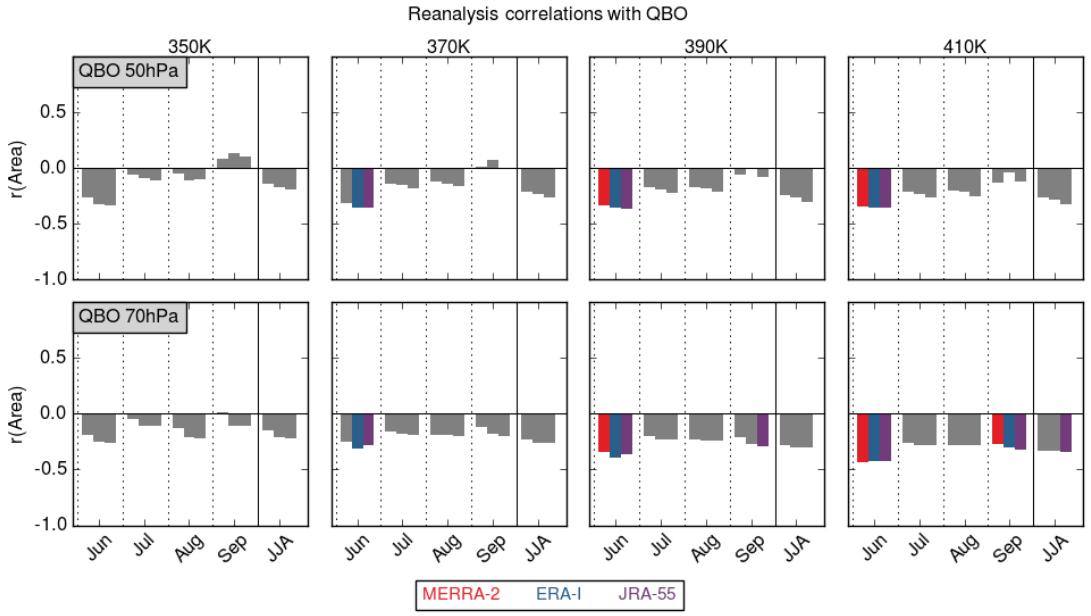

1224 FIG. 13. Correlations between ASMA area and the QBO index defined by Singapore winds at 50 hPa (top)
1225 and 70 hPa (bottom). Correlations that are significant at the 95% confidence level are shown in the reanalysis
1226 colors.

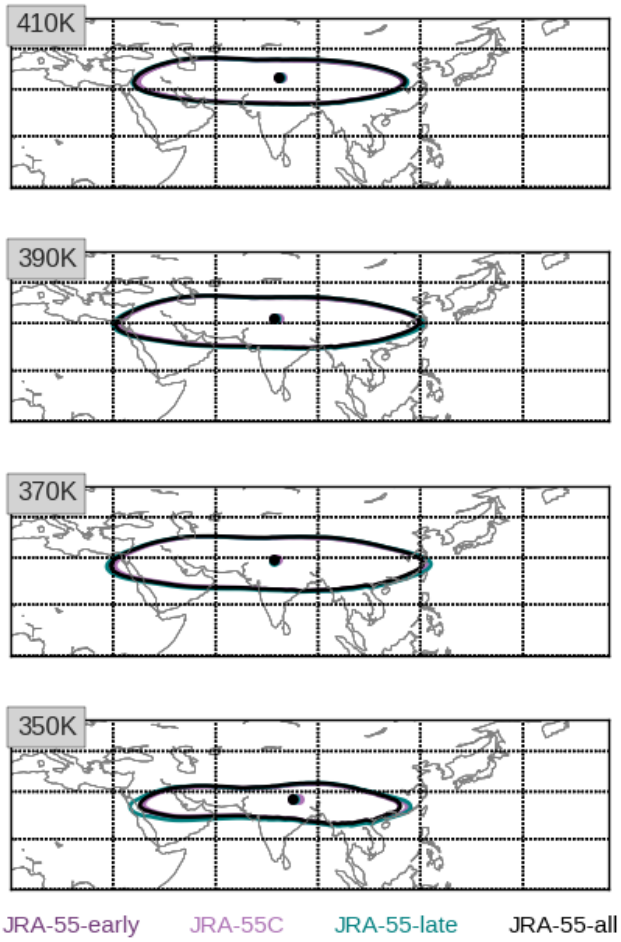

1227 FIG. 14. JJA climatological ASMA edge and centroid values: JRA-55 & JRA-55C for 1973–2012 (purple &
1228 light purple, respectively), JRA-55 for 1979–2018 (teal), and JRA-55 for 1958–2018 (black).

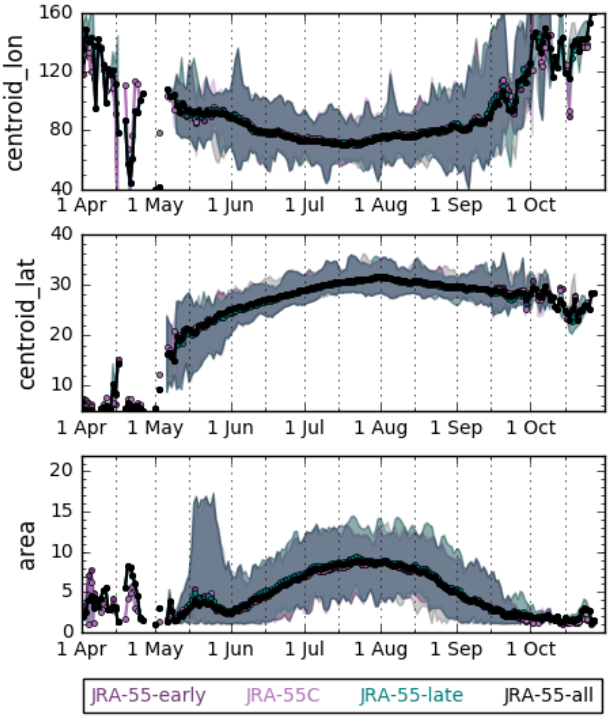

1229 FIG. 15. 370 K climatological (top to bottom) centroid longitude, centroid latitude, and area time series for
1230 JRA-55 & JRA-55C for 1973–2012 (purple & light purple, respectively), JRA-55 for 1979–2018 (teal), and
1231 JRA-55 for 1958–2018 (black).

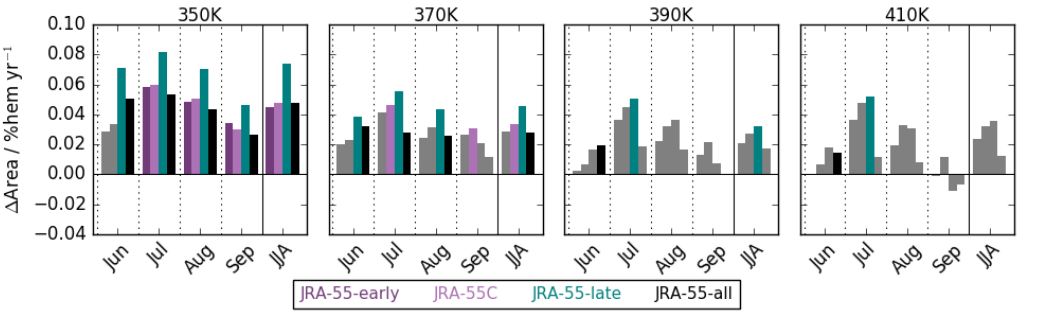

FIG. 16. Slopes of linear fits to the area time series shown in Figure 15. Bars in the reanalysis colors indicate slopes that are significant at the 95% confidence level.

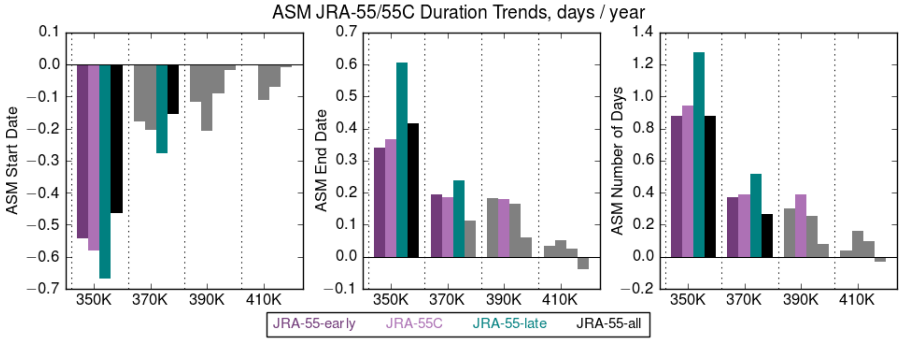

FIG. 17. Changes in ASMA start and end dates and number of days; time periods and colors are as in Fig. 14. Bars in the reanalysis colors show changes that are significant at the 95% confidence level.